

# DIRECTIONAL SPECTRA OF WIND-GENERATED WAVES

By M. A. DONELAN<sup>1</sup>, J. HAMILTON<sup>2\*</sup> AND W. H. HUI<sup>2</sup>

<sup>1</sup> National Water Research Institute, Canada Centre for Inland Waters,  
Burlington, Ontario L7R 4A6, Canada

<sup>2</sup> Department of Applied Mathematics, University of Waterloo, Waterloo,  
Ontario N2L 3G1, Canada

(Communicated by R. W. Stewart, F.R.S. – Received 29 November 1983)

## CONTENTS

	PAGE
1. INTRODUCTION	510
2. EXPERIMENTAL ARRANGEMENTS	513
2.1. Field site	513
2.2. Array design	515
2.3. Wave staffs	516
2.4. Meteorological measurements	518
2.5. Summary of data	518
3. METHOD OF ANALYSIS	520
3.1. Introduction	520
3.2. The modified Barber method	522
3.3. Algorithm for choosing inversion points	523
3.4. Polar analysis	525
4. TYPICAL DIRECTIONAL SPECTRA	527
4.1. Field wavenumber-frequency spectra	527
4.2. Laboratory wavenumber-frequency spectra	531
5. THE FREQUENCY SPECTRUM	531
5.1. Introduction	531
5.2. The rear face	533
5.3. The parameters of the spectrum	535
5.4. Non-dimensional fetch and energy	538
5.5. Comparison with other spectra	539
6. WAVE DIRECTION AGAINST WIND DIRECTION	539
7. PHASE SPEED	541
7.1. Introduction	541
7.2. Average phase speed	541

\* Present address: Vickers O.-Offshore, John Brown House, 20 Eastbourne Terrace, London W2 6LE, U.K.

7.3. Phase speed of free waves	544
7.4. Phase speed of bound harmonics	544
7.5. Amplitude dispersion and Doppler shift of laboratory waves	546
7.6. Amplitude dispersion of field waves	549
<b>8. DIRECTIONAL DISTRIBUTIONS OF WAVE ENERGY</b>	<b>551</b>
8.1. Introduction	551
8.2. The $s$ parameter	551
8.3. The $\text{sech}^2(\beta\theta)$ spreading function	554
8.4. Dependence on $\omega/\omega_p$	556
8.5. The directional spread of the forward face	558
<b>9. CONCLUDING REMARKS</b>	<b>558</b>
<b>REFERENCES</b>	<b>560</b>

From observations of wind and of water surface elevation at 14 wave staffs in an array in Lake Ontario and in a large laboratory tank, the directional spectrum of wind-generated waves on deep water is determined by using a modification of Barber's (1963) method. Systematic investigations reveal the following: (a) the frequency spectrum in the rear face is inversely proportional to the fourth power of the frequency  $\omega$ , with the equilibrium range parameter and the peak enhancement factor clearly dependent on the ratio of wind speed to peak wave speed; (b) the angular spreading  $\theta$  of the wave energy is of the form  $\text{sech}^2(\beta\theta)$ , where  $\beta$  is a function of frequency relative to the peak; (c) depending on the gradient of the fetch, the direction of the waves at the spectral peak may differ from the mean wind direction by up to  $50^\circ$ , but this observed difference is predictable by a similarity analysis; (d) under conditions of strong wind forcing, significant effects on the phase velocity caused by amplitude dispersion and the presence of bound harmonics are clearly observed and are in accordance with the Stokes theory, whereas (e) the waves under natural wind conditions show amplitude dispersion, but bound harmonics are too weak to be detected among the background of free waves.

## 1. INTRODUCTION

Directional spectra of wind-generated waves find application in fields as diverse as basic air-sea interaction, upper mixed layer dynamics, practical wave forecasting, satellite surveillance and engineering design of marine structures and vehicles. This paper attempts to provide a carefully documented description of the purely wind-generated wave directional spectrum derived from lake data which is free of residual wave energy (swell). Laboratory spectra are used to extend our understanding of strongly forced natural waves.

By far the most widely used and accepted method of studying wind waves has been by examination of the spectra of single point time traces of the wave surface elevation. This has been born of the recognition that observed sea states require a statistical description, and that the theoretical shape for waves of small amplitude is a sinusoid (Airy 1845). Hence, by the principle of linear superposition, the spectral representation is a natural description of wave kinematics.

The form of the nonlinear correction to the sinusoidal form of water waves was first computed by Stokes (1847). This correction predicts the familiar narrow high crest and broad shallow

trough intuitively recognized in observations of wind-generated waves, together with an associated increase in the wave phase speed. In terms of the spectral representation, this would appear as enhanced energy at frequencies equal to integral multiples of the wave spectral peak frequency and alterations in the distribution in wavenumber space of the directional spectrum.

As soon as nonlinear features begin to be discussed, however, the principle of superposition is no longer applicable and the spectral representation, although still possible, must be treated with care, especially when seeking to interpret any higher-order features that may be present. Indeed, it has been shown by Whitham (1967) that the amplitude dispersion introduced by the Stokes correction to the phase speed will tend to destabilize a train of uniform parallel crested waves. Thus, the wave spectrum should not be regarded as representing a permanent description of the sea state which would be maintained in the absence of wind forces and viscous dissipation. Instead the spectrum will be in a state of flux through nonlinear interaction of the various spectral components.

Fortunately, however, the second-order nonlinear or Stokes interactions do not result in large frequency shifts of the wave energy. The instability of a Stokes wave train was first discovered by Brooke Benjamin (1967) as a 'side band' instability which would eventually cause wave breaking but could not transfer energy to other than adjacent frequencies.

Phillips (1960) has shown that the third-order nonlinearities that transfer energy from three waves to a fourth, are the first ones that can cause continuous energy transfer over large frequency intervals to a free wave. The size of this transfer was first computed by Hasselmann *et al.* (1973), and has been the subject of many papers: Hasselmann (1962, 1963 *a, b*), Fox (1976), Longuet-Higgins (1976), Korvin-Kroukovsky (1967), Zakharov (1968), Webb (1978), Dungey & Hui (1979). In the last reference it was also shown that a good knowledge of the directional spectrum is required for the nonlinear energy transfer to be calculated accurately. However, because of their high order, these interactions are only of importance when discussing the evolution of the wave spectra with time or fetch. Observations of wave spectra at a particular point in time and space might be supposed to exhibit principally features associated with linear wave theory and the Stokes corrections to it. However, to verify that this is indeed the case requires knowledge not simply of the one-dimensional frequency spectrum but of the three-dimensional directional spectrum which describes the wavelength and directional distributions of each frequency component. For this reason and others associated with the practical matter of wave forecasting, much attention has recently been paid to obtaining estimates of the directional spectrum of wind-generated waves.

Barnett & Kenyon (1975), in a review of the study of wind waves, discussed the methods then available for the measurement of directional spectra. At that time, some measurements had been made of what we call the two-dimensional spectrum, i.e. the one in which the radian wavenumber  $k$  and the (radian) frequency  $\omega$  were assumed to satisfy the linear dispersion relation on deep water

$$\omega^2 = gk. \quad (1.1)$$

Using aerial photogrammetry, Cote *et al.* (1960) obtained the first wavenumber (two-dimensional) spectrum. But, apart from a pioneering attempt by Garrett (1970), who obtained four spectra, no systematic attempt to explore the properties of the full three-dimensional (wavenumber-frequency) spectrum had come to light.

Since that time, a completely new family of methods has become available for measuring

the two- and three-dimensional spectra, namely, remote techniques (see, for example, Tyler *et al.* 1974; Wu 1977; Schuler 1978; Fontanel & de Staerke 1980; Mcleish *et al.* 1980; Pawka *et al.* 1980; Trizna *et al.* 1980; Holthuijsen 1981; Irani *et al.* 1981). Among the established methods reported by Barnett & Kenyon (1975) are those that use the pitch-roll and cloverleaf buoys (Longuet-Higgins *et al.* 1963; Mitsuyasu *et al.* 1975; Hasselmann *et al.* 1980), and the measurements from an array of wave staffs. The disadvantage of the pitch-roll and cloverleaf buoys is that only the first few Fourier coefficients of the angular distribution of the spectral energy density can be determined. The present study was done with an array of 14 wave staffs, thus allowing the calculation of much finer detail in the directional distribution, at some cost in computer time.

The investigation began in 1975 when a tower was built at the western end of Lake Ontario to record wave and wind data to determine the directional spectrum of wind-generated waves. Complementary laboratory experiments of wind-generated waves were done in the large wind-wave tank of the Canada Centre for Inland Waters. Effects of surface tension and finite depth of water will be neglected throughout this paper as the waves observed and discussed here fall into the range of deep water gravity waves.

Our primary purposes in conducting this study were to:

- (i) determine the dispersion relation appropriate to natural wind waves;
- (ii) describe the fetch-limited frequency spectrum in terms of a small number of parameters;
- (iii) find a parametric representation for the spreading function of the directional distribution;
- (iv) use laboratory data to extend the parameter range of field observations.

In addition, the data set is of high quality and allows new information to be obtained on many problems previously not resolved, for example, the dependence of the spectral shape parameters on fetch and wave age, a more detailed look at the polar distribution of the spectral density and its dependence on wave frequency and other parameters.

We begin with a discussion of the possible departure of the dispersion relation of wind waves from the limiting linear relation (1.1). Thus, without wind forcing, the Stokes wave on deep water has been calculated analytically to eleventh order in wave slope  $ak$  of the first harmonic (Hui & Tenti 1982). The surface elevation is given by

$$\zeta = k^{-1} \sum_{n=1}^{\infty} b_n \cos [n(kx - \omega t)], \quad (1.2)$$

where, to fourth order,  $b_1 = ak$ ,  $b_2 = \frac{1}{2}(ak)^2 + \frac{17}{24}(ak)^4$ ,  $b_3 = \frac{3}{8}(ak)^3$ ,  $b_4 = \frac{1}{3}(ak)^4$ . The corresponding dispersion relation is

$$\omega^2 = gk(1 + a^2k^2 + \frac{5}{4}a^4k^4). \quad (1.3)$$

In the limit of infinitesimal waves on deep water, (1.3) reduces to (1.1). For a single train of harmonic waves, any departure from the linear dispersion relation must be caused by one or more of the following effects: (a) finite amplitude; (b) existence of currents; and (c) forcing of the wind.

Comparisons of (1.3) with (1.1) show that the effect of finite amplitude  $a$  or finite slope, is to increase the frequency  $\omega$  for a given wavenumber  $k$  or, equivalently, to decrease the wavenumber (by at most about 20 %) for a given frequency. This is generally called the (local) amplitude dispersion. Another finite amplitude Stokes effect is that the energy of the second

(and possibly higher) harmonic of (1.2) at the peak frequency  $\omega_p$ , say, appears in the wavenumber spectrum at frequencies  $2\omega_p$ ,  $3\omega_p$  etc. These will be called higher harmonic effects. For both effects, the energy density in the wavenumber spectrum for a given frequency will appear inside the linear dispersion circle (1.1) in wavenumber  $\mathbf{k}$  space: the local effect will shift the energy slightly inside the circle by up to about 20%, whereas the higher harmonic effect will shift it at least half-way inside. They are, therefore, quite distinct. In both situations, the effect of finite wave amplitude is to increase the phase velocity.

The water currents in the present investigation are quite small compared with the phase velocity of the wave. Their effects on the dispersion relation are generally insignificant except for laboratory waves. More detailed discussions are given in §7.

The wind pressure that acts on the irrotational wave consists of two parts: one that is associated and correlated with the wave form and the remainder that is random and uncorrelated with the wave form. To determine the effect of the wind pressure on the dispersion relation, only the first part needs to be taken into account. It is found (Phillips 1977, p. 113) that the pressure field in the air  $p_a$  that is correlated with the wave form is necessarily of the form

$$p_a = (\nu + i\mu) \rho_w g \zeta. \quad (1.4)$$

The corresponding dispersion relation for infinitesimal waves is

$$\omega^2 = gk[(1+\nu) + i\mu]. \quad (1.5)$$

The magnitude of  $\mu$ , a measure of the energy input by the wind, is necessarily small under normal generating conditions in nature. On the other hand it can be shown (Phillips 1977, p. 131) that  $\nu$  is less than zero and that its magnitude is also small in most cases, but it has been observed that under very active generating conditions may not be negligible. In those cases, the effect of forcing by the wind is to decrease the frequency for a given wavenumber, or equivalently, to increase the wavenumber for a given frequency. This will move the energy density somewhat outside the linear dispersion circle (1.1) in wavenumber space. It can also be shown (Donelan *et al.* 1983) that once the pressure force  $p_a$  is removed, a forced wave generated by  $p_a$  instantaneously becomes a free wave of the same wavelength but with a sudden decrease in its phase equal to the excess of the forced wave frequency compared with the corresponding frequency of a free wave with the same wavelength.

In a spectrum, Longuet-Higgins & Phillips (1962) have shown that tertiary interactions among components will also produce phase speed changes. However, near the peak of a narrow spectrum, the phase speed changes are dominated by self-interaction of the components near the peak (the Stokes effect discussed above). Fetch-limited wind wave spectra are sufficiently narrow that, as a first approximation, only the Stokes effect need be considered.

## 2. EXPERIMENTAL ARRANGEMENTS

### 2.1. Field site

The map (figure 1) shows the location of the stable platform (a bottom mounted tower: figure 2) in the western end of Lake Ontario. During any given year, Lake Ontario sees several episodes of wind speed in excess of  $15 \text{ m s}^{-1}$ . Its surface temperature varies from about  $1^\circ\text{C}$  in the late winter to about  $20^\circ\text{C}$  in the late summer, and, with an air temperature range

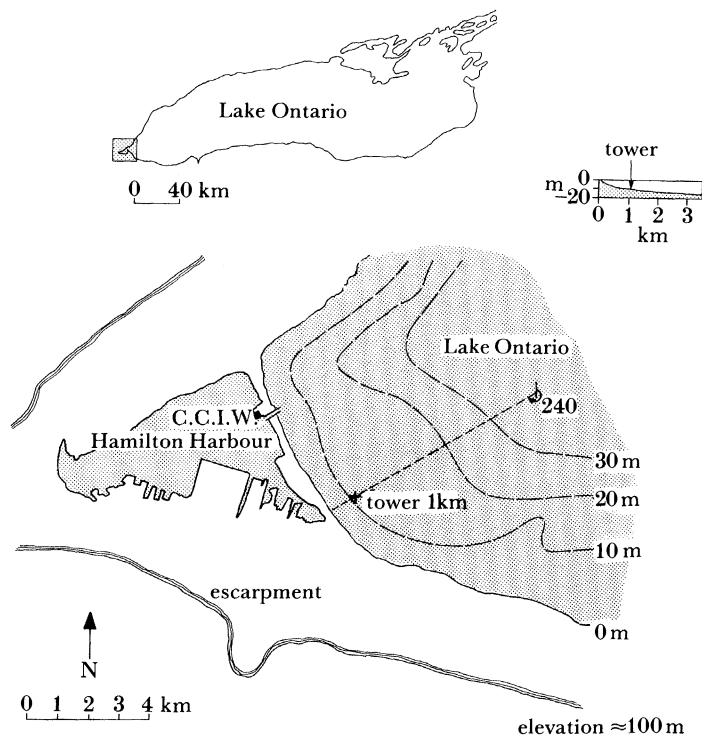


FIGURE 1. Map showing the location of the research tower in Lake Ontario and the shore-normal profile in the vicinity of the tower.

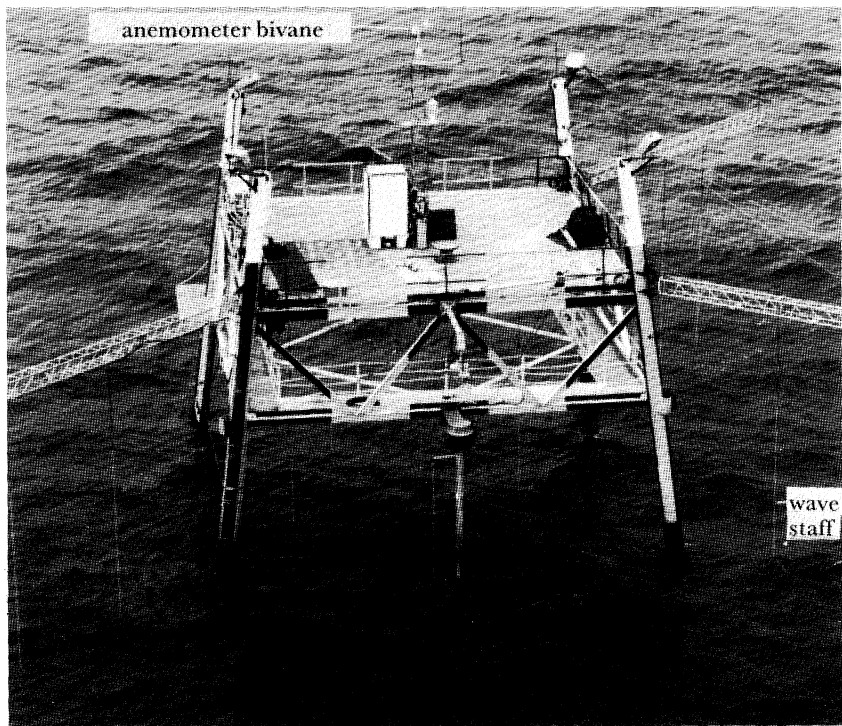


FIGURE 2. Photograph of the research tower. The wave staffs can be seen suspended from the tower itself and from its extensions in three directions. Meteorological instruments are mounted on a mast at the centre and the measuring and communications devices are housed in the box at the foot of the mast.

more than twice as great, near-surface atmospheric stabilities can take on significant non-neutral values even in moderate winds. Although the prevailing winds are westerly and yield fetches of 1.1–2 km, fetches of up to 300 km occur throughout the year.

As indicated in figure 1 (inset), the bottom slopes relatively rapidly (about  $11 \text{ m km}^{-1}$ ) from the shore to the location of the tower at 12 m depth; whereas at and beyond the tower, the bottom slope is gentle ( $1.5 \text{ m km}^{-1}$ ). In addition, the shoreline is very straight and the bottom contours are parallel for 3 km in both directions. The annual variation in water level is less than  $\frac{1}{2} \text{ m}$ ; tides, seiches and wind set-up change the water level by, at most,  $0.1 \text{ m}$ ; there are no significant tidal or seiche currents, and other less organized currents are typically less than  $10 \text{ cm s}^{-1}$ .

The computer-controlled recording equipment (Birch *et al.* 1976) is housed in a trailer onshore, and communication between tower and trailer is by means of an underwater cable.

## 2.2. Array design

At the chosen site, wave periods of up to 4 s are common, with larger peak periods up to 8 s occurring less frequently. Waves having periods in excess of 4 s and, therefore, deep-water wavelengths in excess of 25 m, are modified to some degree by the bottom topography. We, therefore, designed the array for the more common ‘deep-water’ waves (periods less than 4 s). Barber (1963) has suggested that the dispersion relation for surface water waves be invoked to avoid the need for a two-dimensional array. We specifically chose not to follow this piece of advice to be able to determine the extent to which the dispersion relation is modified by nonlinearities in the wave field. Thus the array is in the form of a cross with a maximum extent of 28 m as shown in figure 3.

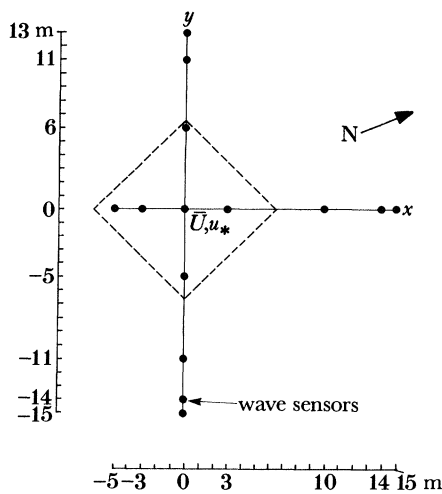


FIGURE 3. Location of wave staffs in the array.

This array allows us to estimate the directional spectra in the manner described by Barber (1963) or Garrett (1970) for waves having wavelengths from 2 to 28 m. The array is oriented so that waves from the longest fetch directions (57–83 degrees true) approach the array at  $45^\circ$  to the arms.

### 2.3. Wave staffs

The 14 wave staffs are of the capacitance type in which the sensing element is a teflon-coated wire 6 m in length. The diameter of the wire is 1.6 mm, and the overall diameter is 4.8 mm. Each wave staff is suspended from the upper deck of the tower, or from one of the arms, by steel cable, and held to a tension of 490 N by rubber 'shock cords' which are anchored to the bottom. The total unsupported length is 18 m with the top support 6 m above mean water level. This arrangement avoids additional attachment structures at mid-depth, which would interfere with the flow field of the waves. The tower itself was constructed with the minimum of cross bracing, and, in fact, is free of any between 3 m above the mean water level and 6 m below. This region is disturbed only by the presence of the four legs of diameter 41 cm, and a fifth smaller pole of ellipsoidal cross section at the mid-point of one side of the tower (see figure 2). The long unsupported length of the staffs has the disadvantage that passage of a wave moves them slightly and hence affects the array configuration. The magnitude of the displacement so produced is roughly proportional to the wavelength of the incident wave and less than 0.3% (about 1 degree phase error) of it for waves that are resolvable by the array.

Among the characteristics of wave staffs of most interest to us were calibration stability, linearity and speed of response. Laboratory tests were done in a transparent pipe (10 cm diameter) in which the water level could be adjusted rapidly. Readings were made at intervals of 1 m, and a linear regression computed. The deviation from the least squares regression line is nowhere greater than 0.33% (Der & Watson 1977) and the slope and intercept of the regression line changed on average by 0.7% and 21 mV (equivalent to 1.3 cm) respectively over four months of field exposure. These laboratory tests established the linearity and stability of the wave staffs, but the actual calibration used was determined in the field by immersing the staffs to various depths near the tower.

The frequency response of the electronic circuitry of the wave staffs was computed and checked by replacing the wave staff with a voltage variable capacitor driven by a sine wave generator. The amplitude response is flat to 30 Hz and the phase shift from 0 to 10 Hz was 1.2° per Hz with a maximum variation of 10% among the 14 staffs. Therefore, the maximum relative phase shift between staffs at frequencies below 5 Hz was less than 1°. The highest frequencies for which we can resolve directional spectra are about 1 Hz for the field and 4 Hz for the laboratory. Much more difficult to establish is the deterioration of frequency response due to the adherence of a film of water to the staff as the water level drops rapidly. A chart recording was made of the output voltage of a wave staff while the water level was dropped in the transparent pipe at the rate of about  $1 \text{ m s}^{-1}$  and then suddenly stopped. The sharpness of the corner, between the decreasing voltage part of the trace and its final constant value, served as an indication of the degree to which the surface film affected the frequency response of the wave staff. Within the time resolution (0.2 s) of the chart recorder used, the corner showed no roundness. It would appear then that the wave staffs were capable of faithful response in the frequency band of interest (0–5 Hz), at least while clean. Evidently algal growth and the accumulation of dirt on the staffs would affect the ability of the teflon to reject water. To reduce this danger, the staffs were cleaned weekly *in situ* with a sponge attached to a rod. As a further precaution, for each run the standard deviations of surface displacement, as indicated by each of the 14 staffs with its own field calibration, were compared with the average standard deviation, and any staff that differed from the average by more than 10% was deemed to be

## DIRECTIONAL SPECTRA OF WIND WAVES

517

dirty or faulty and rejected. The noise level was sufficiently low that no filtering was deemed necessary before A to D conversion. The sharp fall off of the wave spectrum reduced the importance of aliasing. The digitization step (resolution) was 1.5 mm.

At the end of the field observations, a  $\frac{1}{28}$  scaled version of the wave staff array was constructed for use in the wind-wave flume of the Canada Centre for Inland Waters (figure 4). In this case, the sensor was made of a single length of teflon insulated hook-up wire of 1.1 mm outside diameter. Each staff was attached to plywood disks on the top and bottom of the wind-wave flume, and held in 10 N tension. Calibration of the staffs was achieved during filling and emptying of the flume. The same electronic packages were used in both field and laboratory.

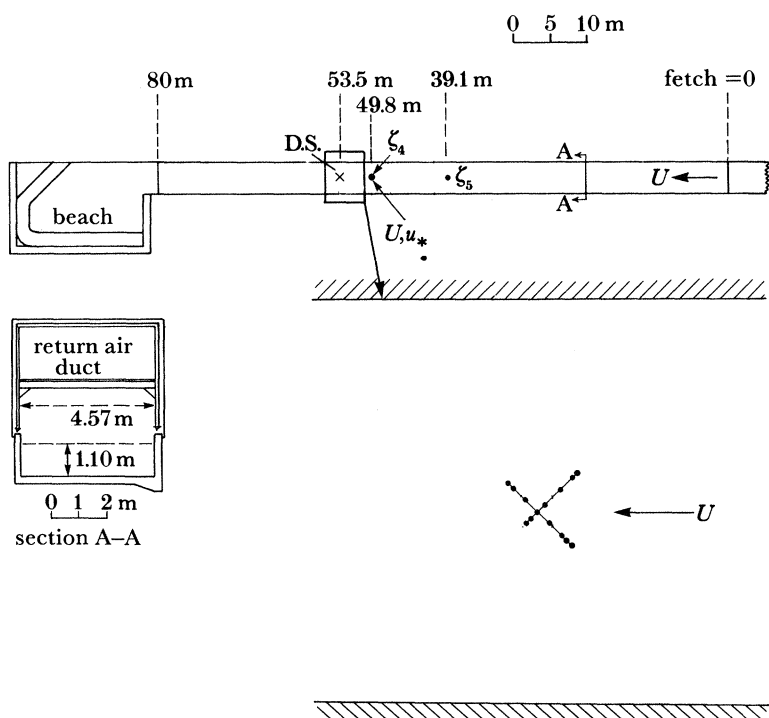


FIGURE 4. Plan of the wind-wave flume. The location of the directional wave array is indicated by an  $\times$  labelled D.S. The lower part of the figure shows an enlargement of the directional array and its orientation in the flume.

In the laboratory, there was some evidence of 60 Hz noise on some of the wave signals. As a result, all the signals were filtered with matched 12 dB per octave Bessel (linear phase shift) low-pass filters, with  $-3$  dB points set at 30 Hz. The sampling frequency was 20 Hz per channel and the maximum resolvable wavenumber  $28 \pi \text{ rad m}^{-1}$ , which corresponds to a frequency of about 5 Hz. The total time delay between channels, caused by the Bessel filter-A to D converter system, was determined by recording a sine wave from a signal generator on all channels simultaneously. At 5 Hz the maximum phase shift between any two channels was  $1^\circ$ . The digitization step (resolution) was 0.4 mm. It has been demonstrated by theory and experiment (Sturm & Sorrell 1973) that surface-intersecting wave gauges effectively average over a circle of diameter much larger than the diameter of the gauge. The effective diameter increases slowly with the gauge diameter and, extrapolating their results, would be about 7 cm for our laboratory gauges, which is the limit of wavelength resolution of our laboratory array.

#### 2.4. Meteorological measurements

At the tower, wind speed, direction and Reynolds stress measurements were made with a Gill anemometer bivane (Gill 1975) mounted at 11.5 m above the water. In addition, air temperature, humidity, water temperature, heat flux and evaporation were also recorded. As an indication of horizontal homogeneity a meteorological buoy was moored about 11.2 km from the tower on a bearing of 60°.

In this paper the wind is characterized by its speed rather than the momentum transfer (or Reynolds stress) to the surface. Since a significant proportion of the stress is supported by very short waves (beyond the limits considered here) it would seem that the wind speed itself is more useful than the friction velocity as a means of characterizing the wind effects on the ‘energy containing’ gravity waves.

#### 2.5. Summary of data

The field experiment was designed to gather sufficient data to describe the directional spectrum of wind-generated waves under a variety of natural conditions. A suitably non-dimensionalized description of the directional spectrum might be expected to be sensitive to non-dimensional numbers descriptive of the general water-air interfacial conditions. It is difficult to conceive of a wind-wave generating process that is unaffected by the relative speeds of wind and waves; thus the parameter  $U/c$ , relating wind speed to wave phase speed, was regarded as the primary ‘sorting’ variable in classifying a population of wind-generated wave spectra. Inasmuch as the wind profile and the intensity of turbulence (hence the pressure fluctuation spectrum) play an important role in the wind-wave coupling problem and are strongly affected by the stability of the atmospheric surface layer, it would seem that a suitable non-dimensional index of stability would be an additional parameter against which to examine the behaviour of the directional spectra. In this paper, we use the bulk Richardson number  $R_b$  as a convenient measure of atmospheric stability, where

$$R_b = Zg(T_a - T_w)/(273 + T_a) U^2.$$

Here  $U$  and  $T_a$  are wind speed and air temperature evaluated at height  $Z$ ;  $T_w$  is the water surface temperature. Finally, the degree of nonlinearity, the tendency towards whitecapping (instability) and the strength of wind-wave coupling are all, to some extent, reflected in the wave slope  $S$ .

We have chosen to classify the data in terms of the atmospheric stability  $R_b$ , an average wave slope  $S$  and the parameter  $U/c$ , which relates wind and wave speeds. Other non-dimensional parameters may be constructed from the variables of the overall flow and geometry, but they are either virtually constant throughout our measurements or unlikely to influence that part of the directional spectrum which is accessible to our observational and computational arrangements.

Clearly, the establishment of the behaviour of the directional spectrum in the three-parameter space defined above would require a large number of measurements of the directional spectra. This led to the design of wholly automatic digital data logging for the field site. However, since each directional spectrum would be calculated from time series of 14 wave staffs sampled at 5 Hz for 14–60 min, some pre-selection of recording times would be required to limit the collected data to a manageable quantity. Our approach was to use a mini-computer to control

the data logging and to decide when to gather data suitable for the computation of directional spectra. The details of the data logging system are described by Birch *et al.* (1976), but a brief summary of the relevant aspects is warranted here. From May 1976 to July 1977, the field site was in operation almost continuously. During most of that time, recordings were made of 1 min averages of wind speed and direction, air temperature and humidity, water temperature and mean square wave height. Every 10 min the average wind speed and air temperature over the previous 10 min were computed and, if they differed by a preset amount from stored reference values, samples, taken five times per second sequentially from each of the channels mentioned above and from all 14 wave staffs, were directly recorded for later processing. This mode of recording of the instantaneous time series for later spectral analysis continued for 1 h, after which the system returned to its normal mode of data logging of the 1-min averages. Ten minutes after this, the reference wind speed and air temperature were updated, and the search for a further change in the wind speed or air temperature continued. It can be seen that this simple method reduced the collection of raw data during periods of steady winds, thereby avoiding repeated realizations of the wave field under very similar overall conditions. By the same token there was, of course, a bias towards changing conditions, but not an overwhelming one, since it was not the rate of change of the wind speed or air temperature which initiated the 'fast' mode but rather the change itself which may have occurred over an hour or several days.

The net product of this scheme was a series of hour-long time series recordings over a wide range of the three parameters of interest. In this paper we are concerned with characteristics of the directional spectrum at steady state. Eighty four runs were analysed, and the overall conditions that prevailed during these runs fell into the following ranges of  $U/c_p$ ,  $R_b$  and  $S$ :

$$\begin{aligned} 0.83 < U/c_p &< 4.6, \\ -0.15 < R_b &< 0.22, \\ 0.005 < S &< 0.020; \end{aligned}$$

$U/c_p$  is referenced to the peak of the spectrum and the wind at 10 m height  $U_{10}/c_p$  and  $S$  is the 'significant slope' as defined by Huang *et al.* (1981a).

There were seven laboratory runs and these are listed separately in table 1 with the values of  $U_{10}/c_p$ ,  $S$  and  $R_b$  also shown. The range of  $R_b$  for these cases is small as the wind-wave flume is not equipped with temperature controls of air or water.

TABLE 1. SUMMARY OF LABORATORY DATA

height/m fetch/m symbol	0.26 $V^a/\text{m s}^{-1}$	10 $U/\text{m s}^{-1}$	$\omega_p/\text{rad s}^{-1}$	$\overline{\zeta^2}/\text{cm}^2$	10 $U/c_p$	53.5 $S(\%)$	0.26 $R_b$
run							
2	3.29	4.58	15.0	0.19	7.5	1.6	+0.011
3	4.80	6.86	11.5	0.55	8.5	1.6	+0.004
5	7.79	11.94	9.0	3.37	11.8	2.4	+0.001
6	9.46	15.40	8.4	5.54	14.0	2.7	+0.001
7	10.87	18.83	7.7	9.56	15.9	3.0	+0.001
29	3.24	4.49	14.9	0.19	7.2	1.6	+0.007
30	12.00	21.88	7.0	20.08	16.5	3.6	+0.001

<sup>a</sup>  $V$  is the measured wind speed.

## 3. METHOD OF ANALYSIS

3.1. *Introduction*

Directional spectra are generally computed from knowledge of the behaviour of the spatial and temporal correlation function. The wave field is assumed to be both stationary and homogeneous and thus, according to the ergodic hypothesis, space and time averages are equivalent to ensemble averages. These will be denoted with an over bar. Thus the covariance of the surface displacement

$$\rho(\mathbf{r}, t) = \overline{\zeta(\mathbf{x}, t_0) \zeta(\mathbf{x} + \mathbf{r}, t_0 + t)} \quad (3.1)$$

depends on the time lag  $t$  and the space lag  $\mathbf{r}$  only. Particular cases of (3.1) are the covariance of the instantaneous surface displacement  $\rho(\mathbf{r}) = \rho(\mathbf{r}, 0)$  and the covariance of the surface displacement at a fixed point  $\rho(t) = \rho(\mathbf{0}, t)$ . Some properties of the self-correlation function  $\rho(t)$  are discussed in Hamilton *et al.* (1979).

The wave spectrum, which is the basic product of our study, is the Fourier transform of  $\rho(\mathbf{r}, t)$

$$X(\mathbf{k}, \omega) = (2\pi)^{-3} \iiint \rho(\mathbf{r}, t) \exp[-i(\mathbf{k} \cdot \mathbf{r} - \omega t)] d\mathbf{r} dt. \quad (3.2)$$

In particular,

$$\overline{\zeta^2} = \iiint X(\mathbf{k}, \omega) d\mathbf{k} d\omega. \quad (3.3)$$

The frequency–direction spectrum  $F(\omega, \theta)$ , our observations of which are discussed in §8, is defined as

$$F(\omega, \theta) = 2 \int_0^\infty X(\mathbf{k}, \omega) k dk, \quad \omega \geq 0, \quad (3.4)$$

where  $\mathbf{k} = (k \cos \theta, k \sin \theta)$ , so that

$$\overline{\zeta^2} = \int_{-\pi}^{\pi} \int_0^\infty F(\omega, \theta) d\omega d\theta. \quad (3.5)$$

Frequently, an approximate directional-frequency spectrum  $F_0(\omega, \theta)$  is derived by assuming the linear dispersion relation (1.1). Thus

$$F_0(\omega, \theta) = 2 \int_0^\infty \delta(k - \omega^2/g) X(\mathbf{k}, \omega) k dk, \quad \omega \geq 0. \quad (3.6)$$

It is this function  $F_0$  that has been the focus of many well-known studies of the directional spectrum (see, for example, Longuet-Higgins *et al.* 1963; Mitsuyasu *et al.* 1975). The frequency spectrum  $\Phi(\omega)$  defined as

$$\Phi(\omega) = 2 \iint X(\mathbf{k}, \omega) d\mathbf{k}, \quad \omega \geq 0, \quad (3.7)$$

is the cosine transform of the self-correlation function  $\rho(t)$

$$\Phi(\omega) = \frac{2}{\pi} \int_0^\infty \rho(t) \cos \omega t dt, \quad (3.8)$$

and in particular

$$\Phi(\omega) = \int_{-\pi}^{\pi} F(\omega, \theta) d\theta \quad (3.9)$$

$$\overline{\xi^2} = \int_0^\infty \Phi(\omega) d\omega. \quad (3.10)$$

An array of  $N$  wave staffs can yield at the most  $N(N-1)+1$  independent point observations of  $\rho(\mathbf{r}, t)$  and, as will become evident, this will not be enough to enable direct estimates of the spectral energy density to be obtained at all the required points. In particular, we have 14 wave staffs (figure 3) yielding (allowing for duplicates) 165 possible spatial points at which  $\rho(\mathbf{r}, t)$  may be determined; whereas the possible resolution is such that we would like knowledge of the spectrum at 2337 locations (see §3.2). Thus, in practice, it is necessary to make assumptions about the location and form of the directional energy spectrum to reduce the number of degrees of freedom of the spectral description to less than the number of pieces of available information. The various methods proposed for evaluating directional spectra may thus be characterized by the objectivity and flexibility of these assumptions.

The method utilized in the present analysis is based initially on the theoretical work of Barber (1963) who described how to obtain a full three-dimensional (or wavenumber–frequency) spectrum  $X(k_x, k_y, \omega)$  from an array of wave staffs. The spectrum, however, is masked by the masking function (or transfer function) of the array of 14 wave staffs. This function will generally be extremely confusing and the information content (degrees of freedom) will still be limited by the number of available staff separations as indicated above. None the less, this procedure was implemented by Garrett (1970) with an array of nine wave staffs, but little quantitative information could be obtained because of the masking function and the limited number of wave staffs used. The method which we have adopted is an extension of the work of Garrett (1970) with post-processing of the masked Barber spectrum to obtain the underlying true spectrum. The method adopted for obtaining the true spectrum with the restricted information available is to choose objectively, by computer algorithm, the locations at which directional energy is observed to be. The amplitude of the spectral energy density is then obtained by a least squares fit to the observed masked wavenumber spectrum. A consequence of this method is that confidence limits for the estimates arise naturally from the fitting process.

Since this method was finalized, a number of papers have been published in which methods of analysing wave staff records to obtain directional spectra are suggested. For example, Davis & Regier (1977) include an extensive discussion of the criteria for array and processing design. However, the main thrust of their argument seems to be obtaining optimal results from relatively sparse data. Comparatively little attention is paid therefore to computational efficiency, and in their companion paper (Regier & Davis 1977) they consider only two-dimensional spectra (satisfying the linear dispersion relation) obtained from an array of six wave staffs. Borgman (1979) proposes both an iterative and a least squares approach for establishing the polar distribution, which approach is similar to that adopted here in the sense that by identifying the location of the energy an improved representation of the distribution can be obtained. However, no attempt is made to suggest methods of either estimating the dependence of  $X$  on  $|\mathbf{k}|$  or of obtaining confidence limits from the estimates obtained. Rikiishi (1978a, b) proposes a direct method for analysing two-dimensional spectra and considers the case  $\omega^2 = \alpha g |\mathbf{k}|$ . Although his method appears to rely on the correct choice of  $\alpha$ , he proposes a test (the detection of wave energy in the opposite quadrant from the major energy concentration) which ‘might’ enable  $\alpha$  to be determined iteratively. However, this procedure does not allow

for the possibility of energy being located at both  $|\mathbf{k}| = \omega^2/g$  and  $|\mathbf{k}| = \frac{1}{2}\omega^2/g$  as would be expected for a Stokes wave.

To summarize, the method adopted for obtaining estimates of the directional spectra (described below) seems to compare well with other methods suggested both before and since its conception. Its advantages are:

- (i) the lack of an assumption about the location and distribution of directional energy, particularly with respect to  $|\mathbf{k}|$ ;
- (ii) the availability of confidence limits for the estimates.

### 3.2. The modified Barber method

All methods of obtaining directional spectra rely on the important relation (3.2). We first do the time Fourier transform of (3.2) to get the wavenumber spectrum  $X(\mathbf{k}, \omega_0)$  at a given frequency  $\omega_0$ . For simplicity, we shall drop the reference to a fixed frequency  $\omega_0$  in the following. Thus  $X(\mathbf{k})$  means  $X(\mathbf{k}, \omega_0)$  and is given by

$$X(\mathbf{k}) = (2\pi)^{-2} \int \int \rho(\mathbf{r}) \exp(-i\mathbf{k} \cdot \mathbf{r}) d\mathbf{r}. \quad (3.11)$$

As in Barber (1963), we obtain the observed or raw Barber wavenumber spectrum.

$$\xi(\mathbf{k}) = \sum_l \bar{\rho}(\mathbf{r}_l) \exp(-i\mathbf{k} \cdot \mathbf{r}_l), \quad (3.12)$$

where the  $\mathbf{r}_l$  are the available separations and  $\bar{\rho}(\mathbf{r}_l)$  is the average of all the estimates of  $\rho$  at each  $\mathbf{r}_l$ .

The distortion introduced by the incomplete information for  $\bar{\rho}(\mathbf{r}_l)$  (the 14 wave staffs yield only 165 independent correlations) can be represented by means of a masking function  $M$

$$\xi(\mathbf{k}) = \int \int X(\mathbf{k}_1) M(\mathbf{k} - \mathbf{k}_1) d\mathbf{k}_1, \quad (3.13)$$

where

$$M(\mathbf{k}) = (2\pi)^2 \sum_l \exp(-i\mathbf{k} \cdot \mathbf{r}_l). \quad (3.14)$$

In figure 5 will be found a contour map of the masking function (by definition  $M(\mathbf{k})$  is real). It will be noticed that (i) there are negative areas; (ii) the two bands along the  $k_x$  and  $k_y$  axes are prominent (related to the arrangement of the wave staffs along orthogonal axes); (iii) the value of  $M(\mathbf{k})$  at  $\mathbf{k} = \mathbf{0}$  is larger than values elsewhere; (iv) the resolution is  $O(\pi/x_{\max})$  and  $O(\pi/y_{\max})$  in the  $x$  and  $y$  directions where  $x_{\max}$  and  $y_{\max}$  are the maximum separations of the wave staffs in the  $x$  and  $y$  directions respectively; and finally, (v)  $M(\mathbf{k})$  is periodic of period  $2\pi$  in  $k_x$  and  $k_y$ . The wave staffs are spaced at 1 m intervals, hence  $\pi$  (28π for the laboratory spectra) is the Nyquist wavenumber.

With the aid of the masking function or array transfer function, the raw wavenumber spectrum can be roughly interpreted and this is the procedure adopted by Garrett (1970) (however, with fewer wave staffs). This is not an acceptable procedure if any systematic analysis is to be done. It is therefore necessary to invert (3.13) to obtain  $X(\mathbf{k})$  directly.

The method adopted was to assume that  $X(\mathbf{k})$  took the form

$$X(\mathbf{k}) = \sum_{m=1}^M E_m \delta(\mathbf{k} - \mathbf{k}_m), \quad (3.15)$$

where the  $\mathbf{k}_m$  are a set of locations ( $m < 165$ ) chosen by using the algorithm described in §3.3. The  $E_m$  are chosen on the basis of a least squares fit to the observed wavenumber spectrum in the region D:  $-\pi < k_x, k_y < \pi$ .

$$\frac{\partial}{\partial E_n} \left\{ \iint_D \left[ \xi(\mathbf{k}) - \sum_{m=1}^M E_m \iint \delta(\mathbf{k} - \mathbf{k}_m) M(\mathbf{k} - \mathbf{k}_1) d\mathbf{k}_1 \right]^2 d\mathbf{k} \right\} = 0, \quad n = 1, 2, \dots, M. \quad (3.16)$$

Evaluating the cross products such as  $\overline{M(\mathbf{k} - \mathbf{k}_1) M(\mathbf{k} - \mathbf{k}_0)}$ , whose calculation is normally required by a least squares fit, would prove lengthy. However, the calculation can be considerably simplified (Donelan *et al.* 1983), and the least squares fit reduced to the set of formulae

$$\xi(\mathbf{k}_l) = \sum_{m=1}^M E_m M(\mathbf{k}_l - \mathbf{k}_m), \quad l = 1, 2, \dots, M, \quad (3.17)$$

these being merely the requirement that the residual is zero at the chosen locations  $\mathbf{k}_l$ .

The steps in this process of recovering the detected wavenumber spectrum  $X(\mathbf{k})$  from the raw (or observed) spectrum  $\xi(\mathbf{k})$  are illustrated in the composite figure 5. This figure was produced by analysing simulated surface elevation time series corresponding to a monochromatic infinite crested wave train travelling along the  $y$  axis in deliberate disregard of the dispersion relation (1.1). Such data should yield delta functions in both frequency and wavenumber space. Figure 5 shows the frequency spectrum, the raw (observed) wavenumber spectrum, the array transfer function and the detected wavenumber spectrum. It can be seen that the raw wavenumber spectrum looks rather like the array transfer function but displaced from the origin along the  $y$  axis. In fact, the raw spectrum is a convolution of the single delta function wavenumber spectrum with the array transfer function. In this case, the inversion process recovered the delta function (within grid resolution) and accounted for 99.88% of the energy in the prescribed spectrum.

Note that the wavenumber spectrum, whatever its shape, is always represented by a set of delta functions. These delta functions may not be located arbitrarily but must be at one of a cartesian array of points

$$\mathbf{k}_m = r \Delta k_x \mathbf{i} + s \Delta k_y \mathbf{j}, \quad (3.18)$$

where  $r, s$  are integers and

$$\Delta k_x = \frac{2\pi}{(2 \times 20 + 1)} m^{-1}; \quad \Delta k_y = \frac{2\pi}{(2 \times 28 + 1)} m^{-1},$$

the maximum staff separations in the  $x$  and  $y$  directions being 20 and 28 m respectively (figure 3). Thus there are  $(2 \times 20 + 1) \times (2 \times 28 + 1)$  (= 2337) possible locations at which values of the directional spectrum are desired in the  $2\pi \times 2\pi$  wavenumber map.

### 3.3. Algorithm for choosing inversion points

The algorithm for choosing the locations  $\mathbf{k}_m$  of (3.15), at which the energy is assumed to lie, is based on the transfer function  $M(\mathbf{k})$  having a strong maximum value at  $\mathbf{k} = \mathbf{0}$ . Thus we proceed as follows:

- (1) The raw energy is calculated from (3.12) at  $41 \times 57$  equally spaced points in  $-\pi < k_x, k_y < \pi$ .
- (2) We find a list of at most 25 locations  $\mathbf{k}_l$ , at which  $\xi(\mathbf{k})$  rises to at least 75% of its maximum value. It would seem reasonable that there is directional energy at these points because of the nature of  $M(\mathbf{k})$ .

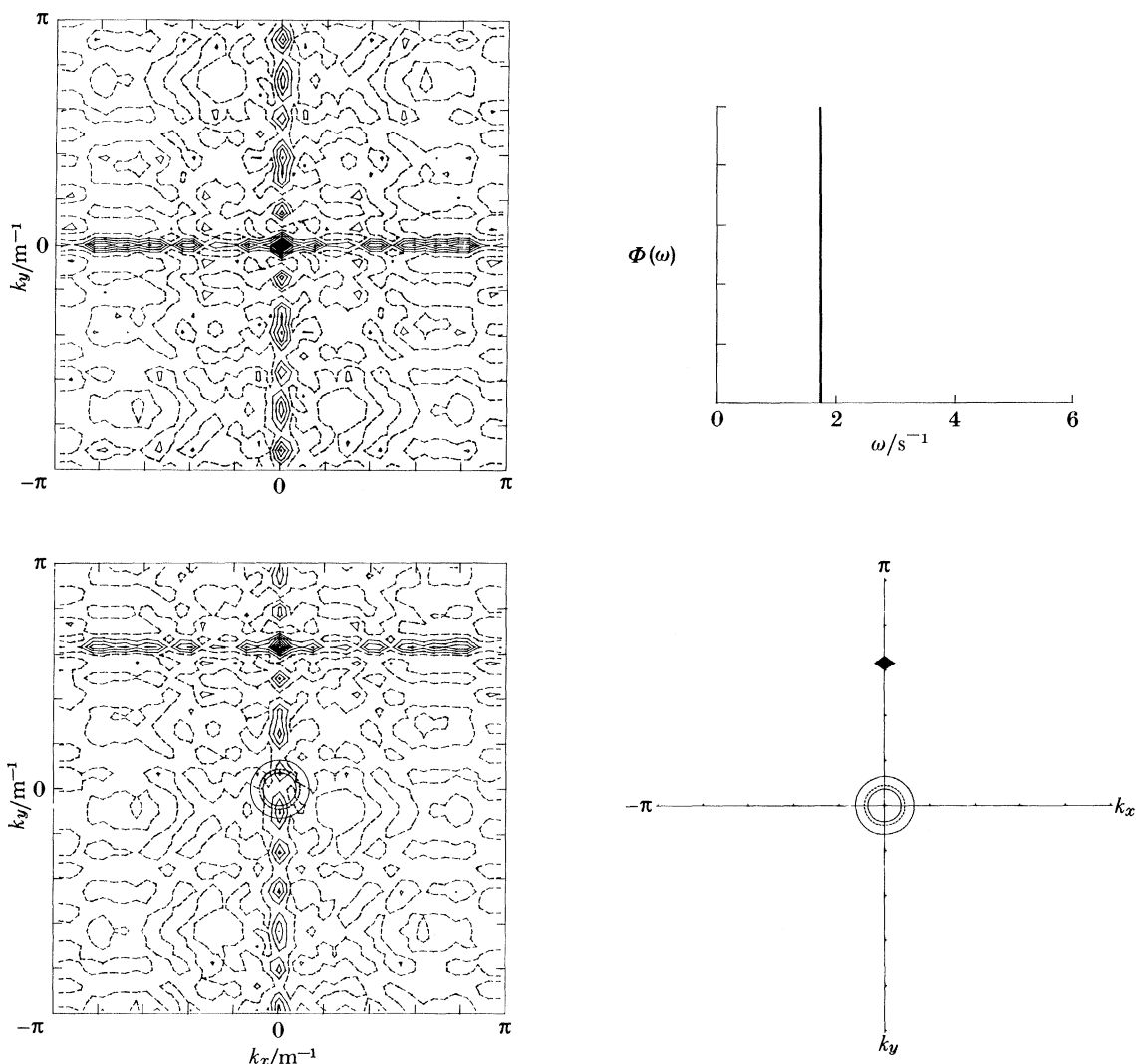


FIGURE 5. A composite figure showing the stages in the process of recovering the detected wavenumber spectrum  $X(\mathbf{k})$ . In this case the data are simulated and correspond to a monochromatic infinite-crested wave train travelling along the  $y$ -axis. The circles correspond to the dispersion relation (1.1) which does not apply to the simulated data. The panels are in anticlockwise sequence from top right: (a) frequency spectrum, (b) array transfer function (or masking function), (c) observed wavenumber spectrum, (d) detected wavenumber spectrum ( $X(k_x, k_y, \omega = 1.75 \text{ s}^{-1})$ ).

- (3) A least squares fit is done to explain the observed  $\xi(\mathbf{k})$ .
- (4) If less than 92.5 % of the variance of  $\xi(\mathbf{k})$  is explained then further searches are made until either a total of 100 points are used or 92.5 % is explained.
- (5) As the order of performing the fitting may influence the values of  $E_m$ , a refit is performed (in batches not exceeding 50 points) to eliminate this bias. This step adds considerably to the computation time required. Note that in this algorithm no use is made of any dispersion relation. Further details of the least squares fitting and the establishment of confidence limits are given in Donelan *et al.* (1983).

### 3.4. Polar analysis

The directional spectrum finds its most frequent application in polar form  $F(\omega, \theta)$ . Formally, this is obtained from  $X(\mathbf{k}, \omega)$  by integrating over all wavenumbers directed along  $\theta$  as in (3.4). Because of the presence of noise at high wavenumbers in  $X(\mathbf{k}, \omega)$ , we cannot integrate over the entire range of  $k$ . Instead we make use of the fact that, in the absence of significant bound energy, the energy in any frequency band clusters around a relatively narrow band of wavenumbers, and we proceed as follows:

- (i) Let  $\delta$  be the width of the band associated with the corresponding frequency bandwidth  $\Delta\omega$

$$\delta \approx 2\omega\Delta\omega/g \quad (3.19)$$

and we set all values of  $E_m$  to zero that do not satisfy

$$||\mathbf{k}_m| - k^*| \leq 2\delta, \quad (3.20)$$

where  $k^*$  is the radius of the wavenumber circle through the  $\mathbf{k}_m$  with maximum associated energy. This procedure is necessary to stabilize estimates for the mean wavenumber  $\bar{k}(\theta)$  as described below.

- (ii) We assume that fitting errors in  $E_1$  and  $E_2$  are all perfectly correlated so that if  $E_3 = E_1 + E_2$  then  $\sigma_3 = \sigma_1 + \sigma_2$ ; where  $\sigma_1$ ,  $\sigma_2$ ,  $\sigma_3$  are the standard deviations of the errors.
- (iii) We then project the energy density  $E_m$  (positive values only) and the zeroth and first moments of the energy, weighted by the standard-deviation estimates  $\sigma_m$  (say) obtained from the fitting procedure, on to a wavenumber circle to obtain  $F(\omega, \theta)$ ,  $M_0(\theta)$  and  $M_1(\theta)$ .
- (iv) These quantities are then binomially smoothed until the half-height width of the influence of a single  $E_m$  just exceeds  $20^\circ$ .
- (v) The mean wavenumber can then be obtained from

$$\bar{k}(\theta) = M_1(\theta)/M_0(\theta). \quad (3.21)$$

Here  $F(\omega, \theta)$  and  $\bar{k}(\theta)$  are the two main quantities of interest, and may be found presented in figure 6. Also plotted are estimates of the standard deviation of  $F(\omega, \theta)$  (obtained in the same manner as the  $F(\omega, \theta)$  but using  $\sigma_m$  instead of  $E_m$ ) and similar graphs calculated by using any negative values that may be present. The graphs, obtained from the negative values, represent an independent estimate of the errors. We have the further check that the total positive energy resolved should be close to the energy content in the frequency band.

As the frequency spectrum  $\Phi(\omega)$  is most easily obtained, it is customary to represent the directional-frequency spectrum by:

$$F(\omega, \theta) = \Phi(\omega)h(\theta). \quad (3.22)$$

It follows from (3.5) and (3.10) that

$$\int_{-\pi}^{\pi} h(\theta) d\theta = 1. \quad (3.23)$$

The method of analysis adopted yields compact polar distributions of the energy. It is preferable, therefore, that the representations adopted for  $h(\theta)$  retain this quality. Previous representations, notably the  $\cos^{2s}(\frac{1}{2}\theta)$  of Mitsuyasu *et al.* (1975) and later Hasselmann *et al.* (1980), were designed to represent directional spectra obtained in the form of a limited number of Fourier coefficients. These distributions are therefore not compact. In figure 7 will be found

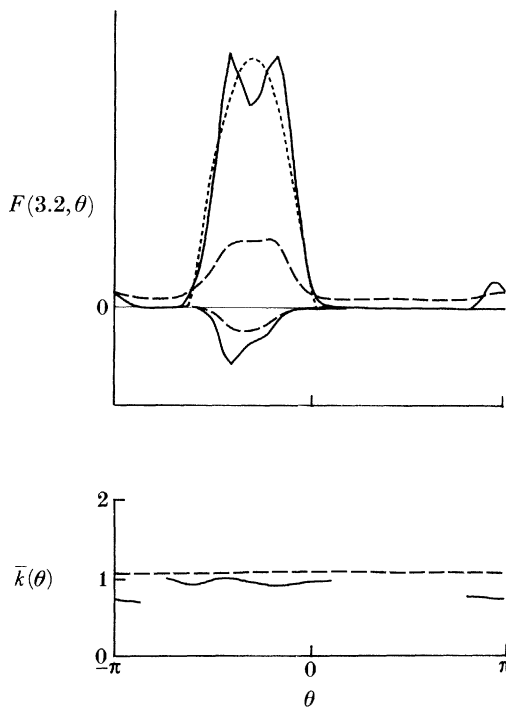


FIGURE 6. The top part of the figure is the directional spectrum corresponding to the wavenumber spectrum of figure 9(d): —, the detected directional spectrum; ---, the parametric fit described in §3.4; -·-, the estimated standard deviation of the directional spectrum. The lower part of the figure is the average wavenumber deduced from the wavenumber spectrum of figure 9(d). The horizontal dashed line corresponds to the linear dispersion relation (1.1), for the frequency of this band  $\omega = 3.2 \text{ s}^{-1}$ .

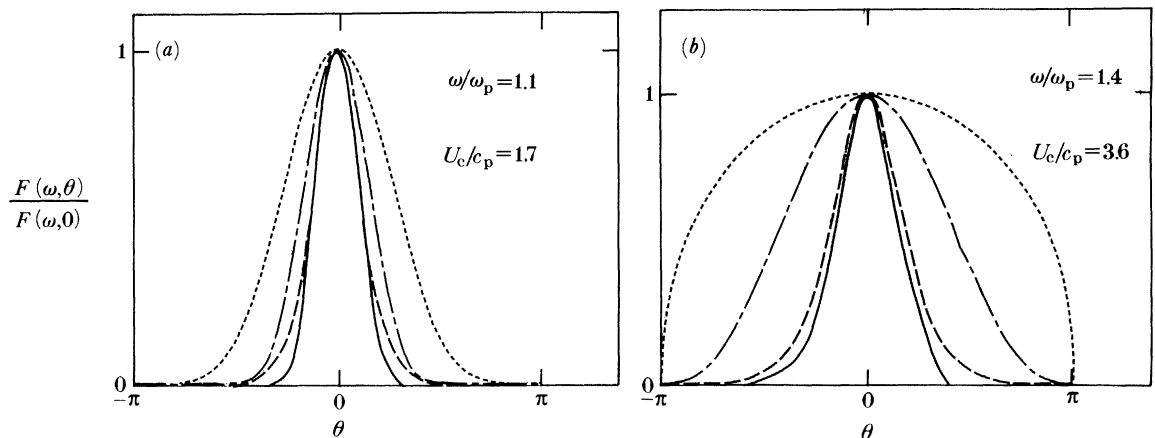


FIGURE 7. Typical directional spectra (—) with polar representations due to Mitsuyasu *et al.* (1975) (---); Hasselmann *et al.* 1980 (—·—);  $\text{sech}^2(\beta\theta)$  (—), see §8.

a typical polar distribution with  $\cos^{2s}(\frac{1}{2}\theta)$  distributions superimposed. Also shown is the distribution described in §8. The polar representations of Mitsuyasu *et al.* (1975) and Hasselmann *et al.* (1980), both deduced from buoys, appear to broaden too quickly with increasing  $\omega/\omega_p$ . Possible reasons for this are discussed in §8. In addition, double-peaked distributions of  $h(\theta)$  were occasionally observed. In these cases, cosine distributions would not be appropriate.

## DIRECTIONAL SPECTRA OF WIND WAVES

527

To avoid placing too stringent controls on the shape of  $h(\theta)$  while, at the same time, smoothing out some of the sampling variability inherent in any spectral decomposition, we devised (Donelan *et al.* 1983) a four-parameter fit to the observed  $h(\theta)$ . The parameters were direction and height of the peak, width and flatness. The last parameter allowed for multiple peaks. The fitted distributions are symmetrical about the peak direction; the fitted distribution is henceforth described as the ‘test model’. Examples of these fitted  $h(\theta)$  are given in figures 6, 27 and 28. This set of four parameters per spectrum was then used (§8) to select an average shape function  $h(\theta)$ .

## 4. TYPICAL DIRECTIONAL SPECTRA

4.1. *Field wavenumber-frequency spectra*

In this section, we present and discuss some representative wavenumber spectra calculated from wind-wave data recorded in Lake Ontario during 1976–1977. In all these calculations, the wave fields are assumed to be stationary and homogeneous.

In each of the two cases to be presented (figures 8 and 9), we show a frequency spectrum and a sequence of wavenumber spectra  $X(\mathbf{k})$  for frequency bands of width  $\Delta\omega$ . In these plots, the solid circles represent the limits of the deep-water dispersion relation (1.1) for infinitesimal waves and correspond to the limits of the frequency bands analysed, whereas the broken circle corresponds to the (energy) centroidal frequency of the band.

All the waves analysed have wavelengths of the dominant wave less than twice the water depth at the tower (i.e. less than 24 m). Hence, finite depth effects on the dispersion relation are negligible. Within the resolution of these contour plots, higher harmonics of the dominant waves are not observed, but they are observed in the laboratory experiments as will be seen below.

In figure 8 near the peak frequency, the energy is concentrated and lies between the two solid circles, which indicates that the linear dispersion relation (1.1) is obeyed for those waves which are near full development,  $U/c_p = 1.5$ . At higher frequencies, the energy density appears slightly inside the inner solid circle. This could be due to the local Stokes effects of finite wave slope. As discussed in §1, such effects can cause a departure from the linear dispersion circle by up to about 20 %. Figure 9, on the other hand, corresponds to younger waves ( $U/c_p = 3.1$ ), i.e. stronger wind generation near the peak frequency. It can be seen that in this case there is evidence of amplitude (finite slope) dispersion just above the peak as well as at higher frequencies.

In a few cases it was observed that the energy density lies outside the larger dispersion circle. This may be explained by the presence of forced waves according to the theory in §1. Actually, one should expect forced waves to be present much more regularly than the directional spectra show. We attribute this lack of evidence of forced waves in the directional spectrum to intermittency of the generation process. It was shown in Donelan *et al.* (1983) that on removal of the forcing, forced waves instantaneously revert to free waves of the same wavelength but with a sudden shift in the phase, and hence, since the spectra represent averages over time and do not retain the phase information, they should be predominated by the free waves, as observed.

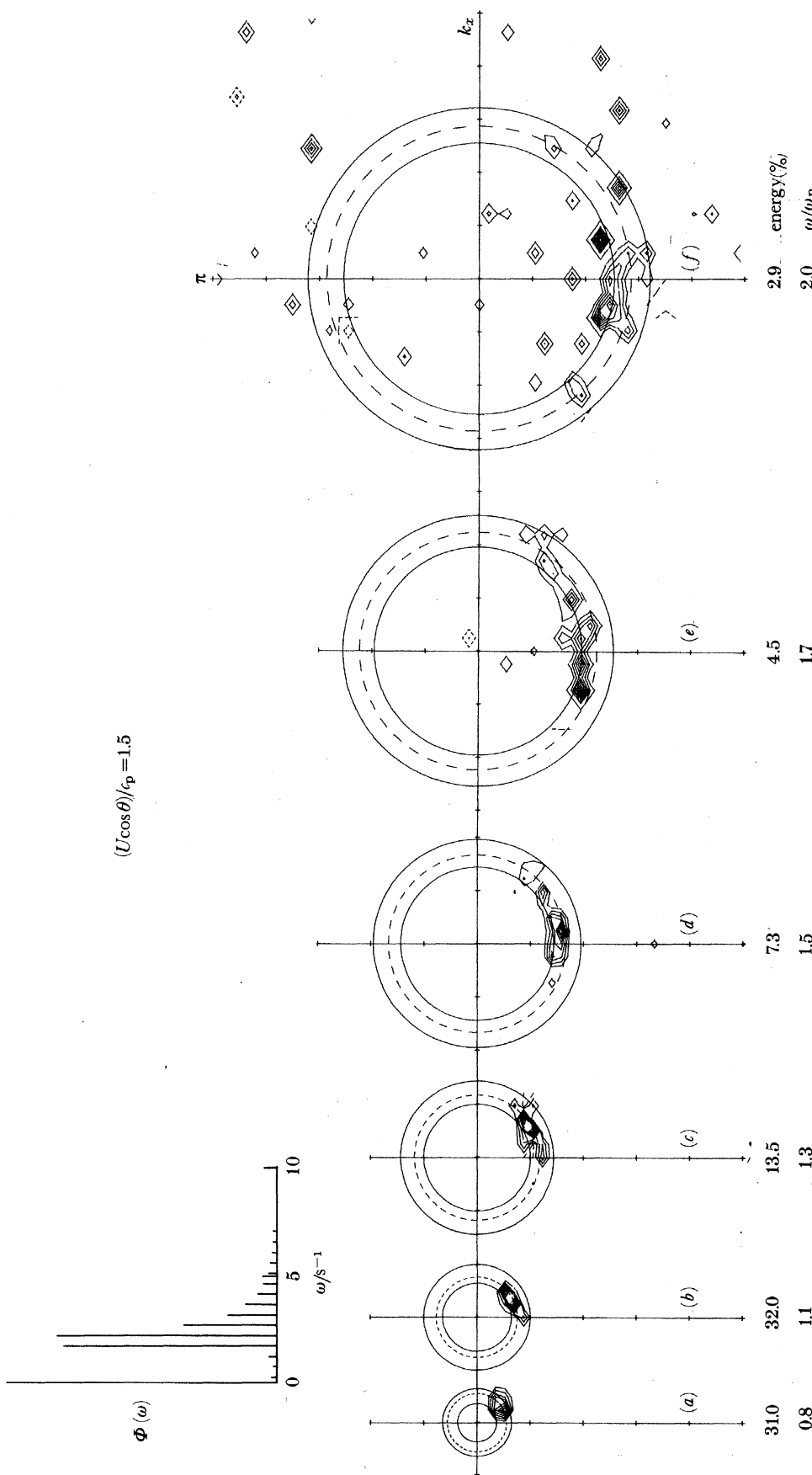


FIGURE 8. Wavenumber spectra  $X(\mathbf{k}, \omega)$  for a relatively mature spectrum of field waves. The fraction of energy in each frequency band is indicated. Note that the energy falls within the dispersion circles near the peak, but moves inwards at higher frequencies. Run number is 339064.

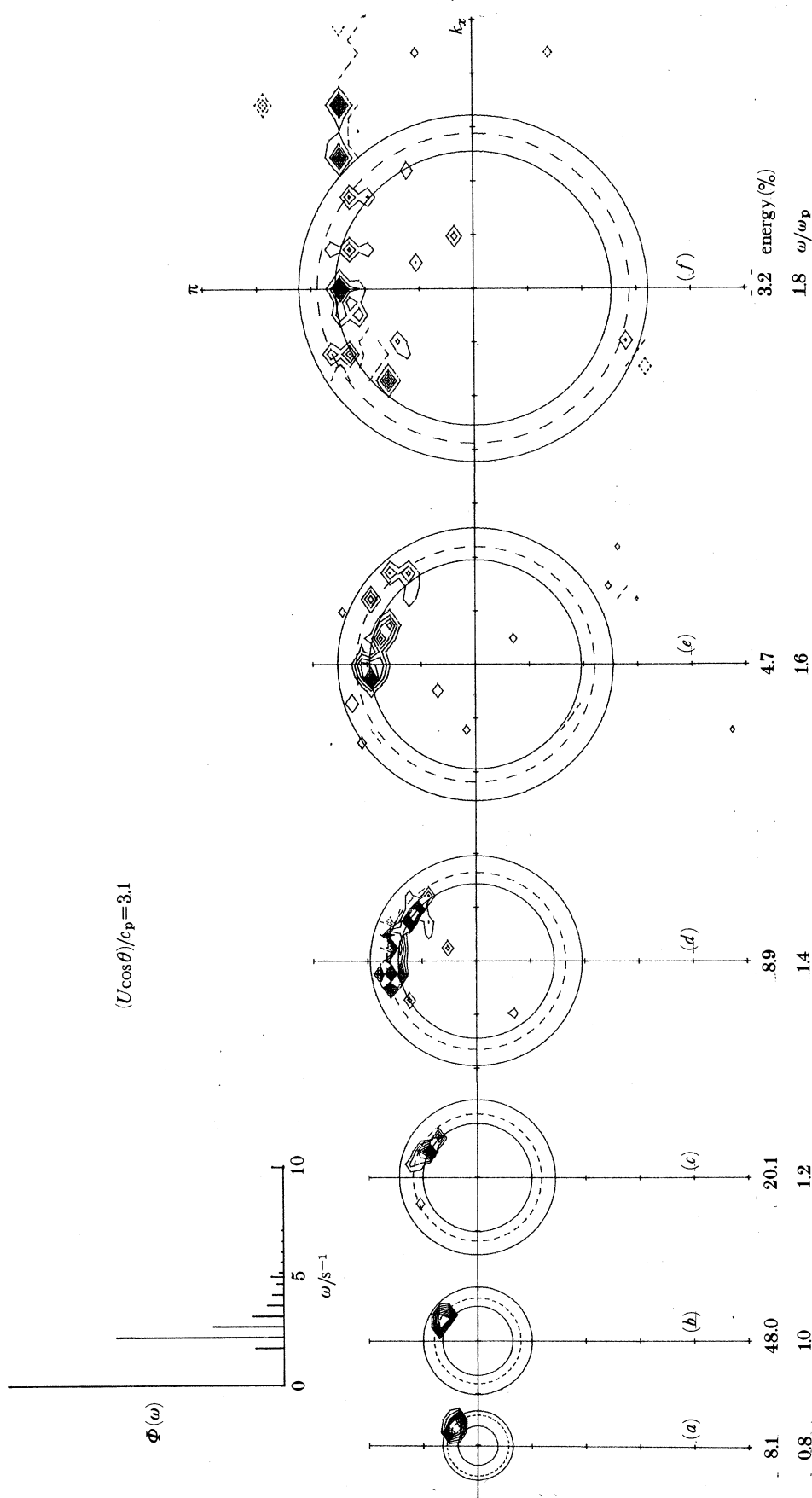


FIGURE 9. Wavenumber spectra for a relatively young spectrum of field waves. Note that the energy contours are closer to the centre than in figure 8. Run number is 128174.

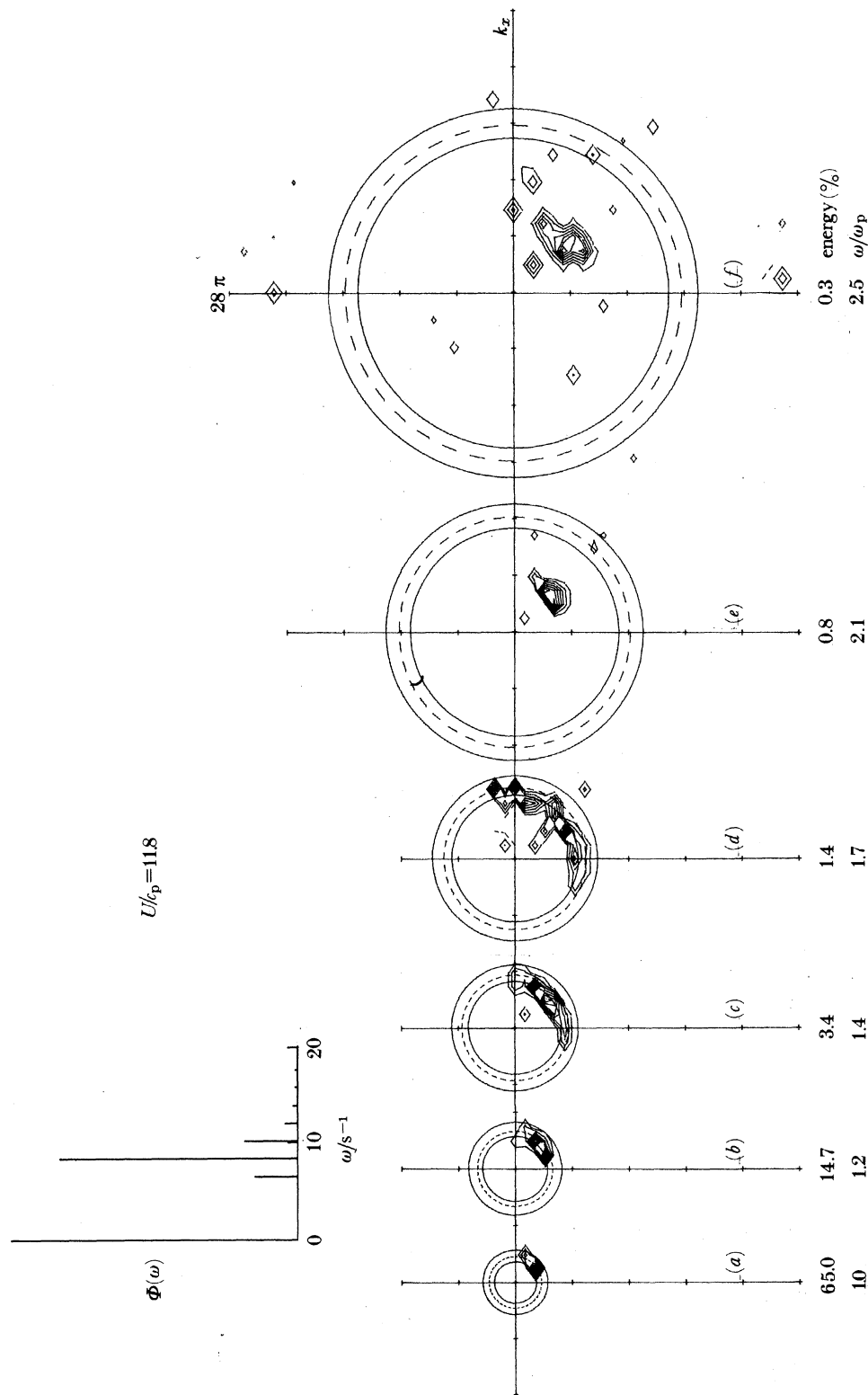


FIGURE 10. Wavenumber spectra for very young laboratory waves. Evidence for bound harmonics can be seen in (d), (e) and (f). Run number is 5.

#### 4.2. Laboratory wavenumber-frequency spectra

Wave data were also recorded in the wind-wave flume at C.C.I.W. with a  $\frac{1}{28}$ th scale array of wave staffs in the same configuration as the tower. In no case was the wavelength of the waves at the spectral peak more than 1.15 times the water depth (1.1 m). Therefore, as for the field data, these laboratory waves are deep water waves. Wavenumber spectra for a typical case (run no. 5) are shown in figure 10 at various frequencies. The frequency spectrum is narrow and the general features of the wavenumber spectra resemble those in the lake, with some very significant differences. Thus, for instance, while at the peak frequency ( $\omega_p = 8.96 \text{ s}^{-1}$ ), the wave energy is nearly on the linear dispersion circle, for higher frequencies, the energy appears progressively inside the circle. As we shall describe in detail in § 7, this is a reflection first of amplitude dispersion and then, at  $\omega/\omega_p = 1.7$ , of the appearance of bound harmonics. In these plots the lowest positive contour is 12.5% of the peak so that the relatively small free wave energy cannot be seen in (e) and (f). The coexistence of free and bound energy is seen clearly in (d).

### 5. THE FREQUENCY SPECTRUM

#### 5.1. Introduction

In this section we examine certain characteristics of the frequency spectrum. We restrict our attention to cases in which there is no swell. In fact, Lake Ontario is smaller than typical meteorological systems and the wave spectra are usually uni-modal with little or no evidence of swell.

Kitaigorodskii's (1962) similarity argument on the scaling of fetch-limited spectra has provided the basis for a consistent description of several sets of field observations and tank experiments (Pierson & Moskowitz 1964; Mitsuyasu 1968, 1969; Liu 1971; Hasselmann *et al.* 1973; Ramamontjarisoa 1973). The success of Kitaigorodskii's scaling law is strong support for the concept of the similarity of fetch development of the wind-generated gravity wave spectrum, which can be completely described by a length scale associated with the fetch, and a velocity scale associated with the source of energy: the wind. Such a description, however, is limited in its practical usefulness to situations in which the fetch is known and the wind is relatively constant along the fetch. In the general case of winds variable in speed and direction, a description of the parameters of the spectrum in terms of local conditions would be valuable. Therefore, instead of the non-dimensional fetch  $\tilde{x} = xg/U^2$ , we have chosen to relate the spectral parameters to  $U_c/c_p$ , the ratio of the component of the 10 m wind speed in the direction of the waves at the peak of the spectrum to the phase speed of those waves.

In figure 11 we have collapsed the frequency spectra for all the cases on to axes normalized by the magnitude of the peak spectral density and of the peak frequency. The spectra have been grouped into classes by the parameter  $U_c/c_p$ . The 90% confidence limits based on the standard errors of the mean, in each band of width 0.1, are indicated at the top of the figure. The position of the vertical bar indicates the average value of  $\omega/\omega_p$  in each band. It appears that there is a pronounced narrowing of the spectra with increasing  $U_c/c_p$ . The smooth variation in width and otherwise smooth variation of the spectra support the idea that wind-generated spectra may be described in a similarity framework such as that proposed by Kitaigorodskii (1962) and applied with dramatic effect by Hasselmann *et al.* (1973).

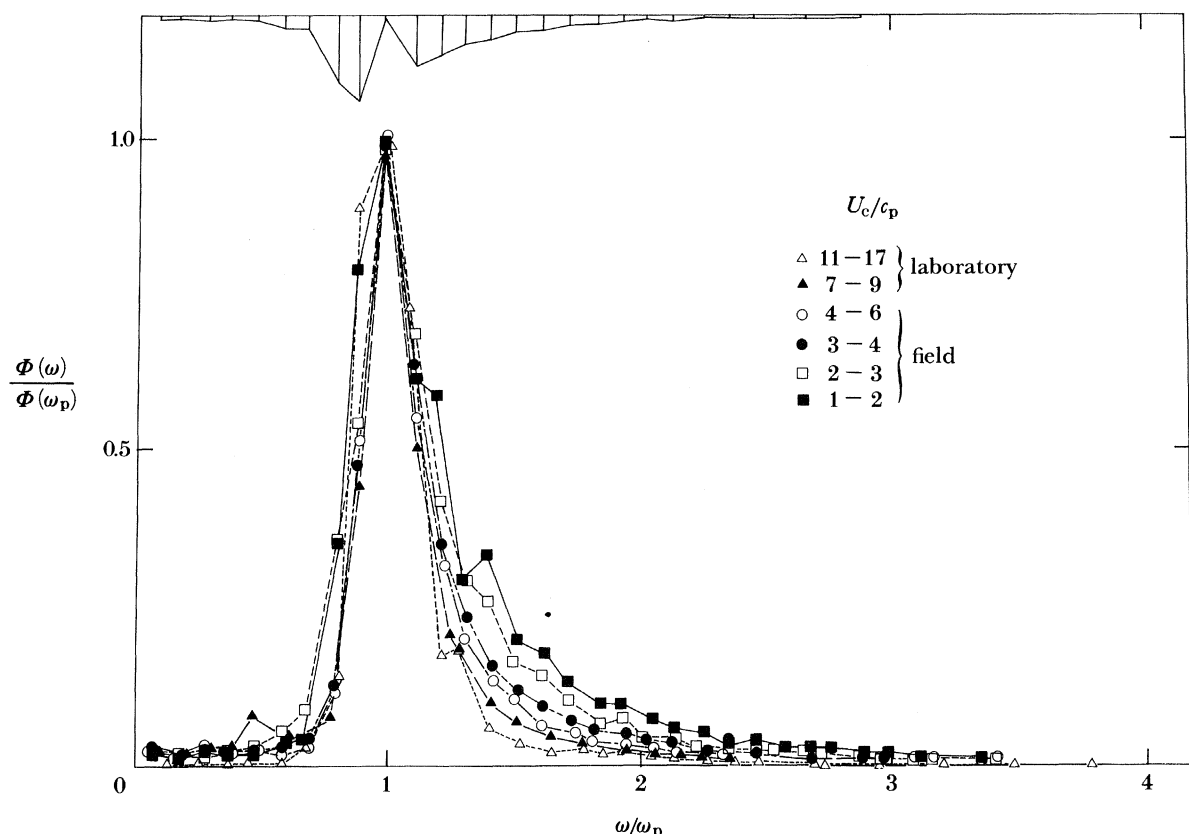


FIGURE 11. Normalized frequency spectra grouped into classes by  $U_c/c_p$ . The vertical bars at the top of the figure are an estimate of the 90 % confidence limits based on the standard error of the mean.

Spectra normalized in this way provide useful summaries of the observed process provided that the estimates of the normalizers, peak frequency and spectral peak, are accurately determined. Donelan & Pierson (1983) have shown that errors in estimation of the peak frequency and the spectral value there may arise if the confidence limits on the spectra are not sufficiently narrow. Each of the 16 spectral estimates from each of the staffs contains 256 degrees of freedom corresponding to 90 % confidence limits of  $\pm 15\%$ . The frequency spectra discussed here are averages of all 14 wave staffs so that the number of degrees of freedom per estimate is increased by a factor between 1 and 14 depending on the wavelength or frequency. In the extreme case of very short waves the 90 % confidence limits are only  $\pm 4\%$ .

As pointed out by Donelan & Pierson (1983), the uncertainty in the measured spectral estimates can lead to error in the selection of the peak frequency. For 90 % confidence limits  $\pm 15\%$  wide and spectral shapes as shown in figure 11 the peak frequency is within  $\pm 5\%$  of its true value 90 % of the time. A more serious error is associated with the coarse frequency resolution: the price paid for close confidence limits on the spectra. That is, if the true peak falls between two spectral estimates it may be as much as 10 % away from either estimate. To compensate for this the peak frequency  $\omega_p$  is taken to be the centroid of the three estimates at and on either side of the measured peak.

### 5.2. *The rear face*

It is generally agreed that wind-wave spectra have a very sharp cut-off at frequencies below the peak, i.e. on the forward face, and a somewhat more gently sloped rear face. Current practice in describing wind-wave spectra owes its origin to the pioneering work of Phillips (1958). He argued that the shorter waves on the rear face of the spectrum are limited in amplitude largely through breaking of their steepest members. Phillips's argument, based on dimensional considerations, suggests that the energy density of the rear face of the spectrum should be inversely proportional to frequency to the fifth power: the so-called  $\omega^{-5}$  power law. He further argued that, although the wave energy in a wind-wave field may grow with time or down fetch, the growth should be largely by the development of the longer waves below the peak without much change to the shorter waves. That is, the rear face of the spectrum could be described by  $\alpha\omega^{-5}$ , where  $\alpha$  is a universal constant. The first attempts to test Phillips's hypothesis (see, for example, Burling 1959; Kinsman 1960) supported the idea of an 'equilibrium range' on the rear face of the spectrum with an  $\omega^{-5}$  behaviour. More recently, however, both the constancy of  $\alpha$  and the  $\omega^{-5}$  frequency dependence have been called into question (Garrett 1969; Longuet-Higgins 1969; Hasselmann *et al.* 1973; Ramamonjiarisoa 1973; Toba 1973; Kitaigorodskii *et al.* 1975; Misuyasu *et al.* 1975; Forristall 1981; Kahma 1981).

Longuet-Higgins (1969) demonstrated that  $\alpha$  is related to the wave age. Hasselmann *et al.* (1973), in a careful study of fetch-limited waves, related  $\alpha$  to the non-dimensional fetch  $\tilde{x} = xg/U^2$ . In these studies the power law that described the rear face of the spectrum varied between  $-3.5$  and  $-5.0$ . It would appear that not only is  $\alpha$  not a constant but the frequency dependence of the rear face may also vary considerably.

Accordingly, as a starting point in describing our spectra we examined them to attempt to determine the characteristics of the rear face of the spectrum. In the 'energy containing' region of the spectrum, i.e. spectral levels greater than 1% of the peak, the rear face of the spectrum is well described by an  $\omega^{-4}$  power law. To illustrate the slope of the rear face the spectra have been multiplied by  $\omega^4$  and normalized by the average level of the spectral estimates multiplied by  $\omega^4$  in the frequency region  $1.5\omega_p < \omega < 3.0\omega_p$  (see figure 12). It is clear that an  $\omega^{-4}$  power law is a good description of the rear face of the spectrum in the energy containing region. For comparison  $\omega^{-5}$  and  $\omega^{-3}$  power laws are also shown. Although harmonic peaks are clearly evident in the largest  $U_c/c_p$  spectral group, the mean spectral level is in good agreement with the  $\omega^{-4}$  line. Both the laboratory and field data support an  $\omega^{-4}$  description of the rear face of the spectrum in the frequency region  $1.5\omega_p < \omega < 3.5\omega_p$  of the wind-generated gravity wave spectrum. Although the result we have quoted is simply an empirical one, there is theoretical support for an  $\omega^{-4}$  equilibrium range in the work of Zakharov & Filonenko (1967).

It is not our purpose here to try to reconcile our observations with the conclusions of the enormous literature of wave spectra that has gone before. We emphasize, however, that we have confined our attention to the energy containing region of the rear face of the wind-generated gravity wave spectrum, because it is here that a simple and accurate spectral description finds frequent and valuable practical application.

The establishment of a power law appropriate to the rear face of the wave spectrum is often troubled by the possibility of Doppler shifting of the spectral estimates by currents (Kitaigorodskii *et al.* 1975). Tidal currents in Lake Ontario are insignificant in this context, and the wind-driven

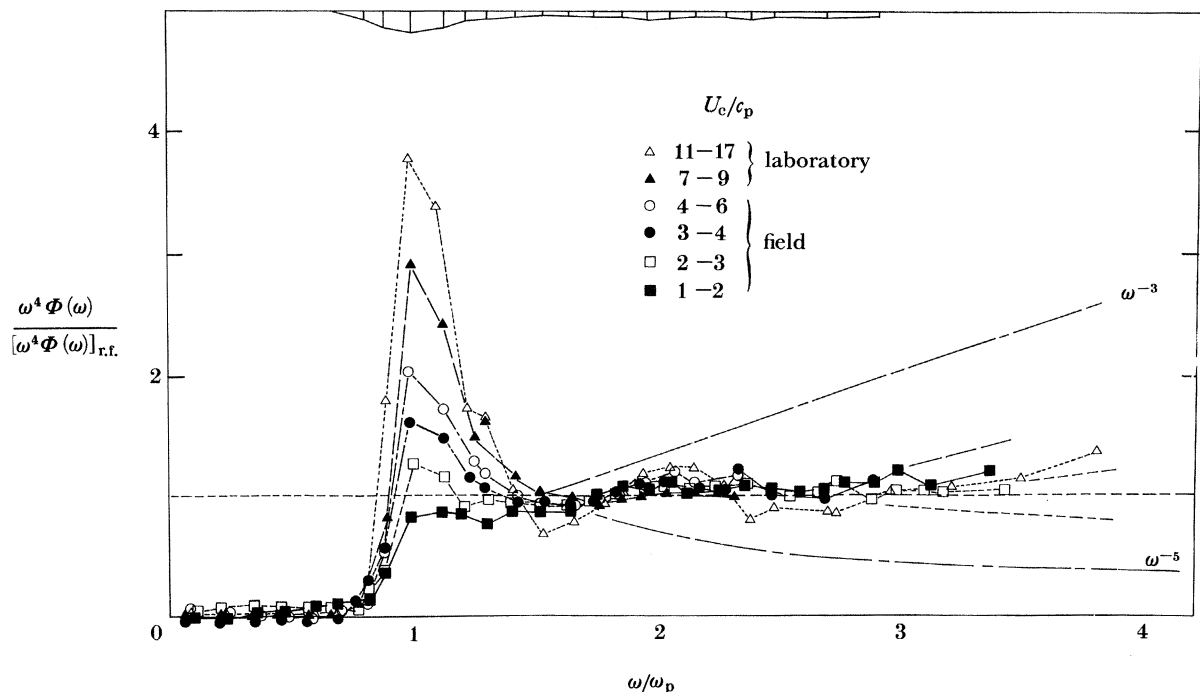


FIGURE 12. Frequency spectra times  $\omega^4$  normalized by the rear face  $[\omega^4\phi(\omega)]_{\text{r.f.}}$  which is the average of  $\omega^4\phi(\omega)$  in the region  $1.5\omega_p < \omega < 3\omega_p$ . The lines corresponding to  $\omega^{-5}$  and  $\omega^{-3}$  are also shown (—). The effect of a  $10 \text{ cm s}^{-1}$  ambient current with or against the waves is also shown (---) as is the effect of wind drift in a  $10 \text{ m s}^{-1}$  wind (—). The spectra are grouped in classes of  $U_e/c_p$ .

and thermal circulation produces upper layer currents that are generally under  $10 \text{ cm s}^{-1}$  (Simons 1974, 1975). The field spectra have been analysed in 16 frequency bands with the lowest and the highest centred on  $0.044 \text{ Hz}$  and  $1.22 \text{ Hz}$  respectively. As a result, the ratio of phase speeds to current speeds is 13 or greater, and the calculations of Kitaigorodskii *et al.* (1975) indicate that the Doppler shift does not alter the slope of the rear face materially. Furthermore, there is no reason to suppose that the direction of the currents and waves are correlated. In fact the waves tend to be offshore or onshore (prevailing wind directions) and the lake currents are inclined to be shore parallel (topography steered). None the less, we have indicated (figure 12) the maximum distortion to the observed  $\omega^{-4}$  slope based on Kitaigorodskii *et al.* (1975) for  $10 \text{ cm s}^{-1}$  currents with and against the waves. We have used their results for the cosine squared distribution since this is in reasonable agreement with the directional spread (§8) at high values of  $\omega/\omega_p$  where the Doppler shift might be important. It appears that the effect on the spectral slope of the ambient currents is not significant in these lake data, and of course does not exist in the laboratory tank data.

Doppler shifting due to surface wind drift may, in some instances, be an important factor. The combination of short waves and strong winds is particularly prone to this source of error, since the current is strongly sheared near the surface and is about 2.5% of the wind speed (Wu 1975). In §7 we demonstrate that in strong surface shear the short waves appear to be advected at a speed corresponding to the current speed at a depth of order  $1/k$ . In figure 12 is indicated an approximate correction for the wind drift (field data) based on an average wind speed of  $10 \text{ m s}^{-1}$  and the wind drift profile inferred by Donelan (1978). It can be seen that this correction is only of importance in these field data for  $\omega/\omega_p > 3$ . Furthermore, correcting for

this source of error would make the spectral slope slightly more negative than  $\omega^{-4}$  for  $\omega > 3\omega_p$  and essentially unchanged for  $\omega < 3\omega_p$ . Evidently an  $\omega^{-4}$  power law provides an excellent description of the rear face of these lake spectra in the energy containing region  $1.5\omega_p < \omega < 3\omega_p$ .

The laboratory spectra show a tendency to increase slope above  $\omega/\omega_p = 3.2$ , which is probably because of wind drift currents. We shall explore this further in § 7. However, we remark that it is difficult to assign a slope to the rear face of the spectrum of the strongly forced ( $U/c_p > 9$ ) laboratory waves, because of the presence of pronounced harmonic peaks (see § 7). Moreover, we are attempting to find a general description for the spectra of natural waves, and are using the laboratory data only to extend the parameter space beyond that able to be realized with our field site. The rationale for this is that the broader parameter ranges thus achieved help us to discern trends that may otherwise be buried in the noise – sampling and geophysical variability – of the field data. At the same time we remain fully cognizant that in many instances the differences between the conditions of the laboratory and lake are sufficient to prevent close quantitative correspondence between them.

Inasmuch as the rear face of both the laboratory and field spectra falls off as  $\omega^{-4}$ , previous spectral shapes based on an  $\omega^{-5}$  rear face, such as the Pierson & Moskowitz (1964) and JONSWAP (Hasselmann *et al.* 1973), are not appropriate. More recently, Huang *et al.* (1981*b*) have proposed a spectral model in which the slope of the rear face is dependent on the ‘significant slope’, an internal parameter of the wave field defined as the ratio of root mean square surface elevation to the wavelength of the spectral peak. While the model of Huang *et al.* provides some flexibility in the slope of the rear face of the spectrum, it does not attempt to describe the peak enhancement independently, deemed so important in the JONSWAP data. In addition, in describing the energy containing region about the peak of the spectrum, their model deviates considerably from the observed behaviour of the equilibrium region.

In this section, additional runs from another laboratory experiment (Donelan 1979) in the same tank were used to supplement the seven directional array runs. These extra data appear in figures 13, 14, 15 and 16. The statistical reliability of these points is less because they are derived from a single wave staff rather than from the average of an array of fourteen. In figures 13 and 14 they are grouped in bands of  $U/c_p$  to compensate for their lower individual reliability than the runs derived from the array.

### 5.3. The parameters of the spectrum

Our spectra are characterized by relatively constant rear face slope ( $\omega^{-4}$ ) and pronounced peak enhancement (figure 12). Accordingly the JONSWAP spectral model, modified to account for the  $\omega^{-4}$  rather than the  $\omega^{-5}$  rear face, would seem a plausible candidate for describing these spectra. The modification consists of replacing  $\omega^{-5}$  by  $\omega^{-4}\omega_p^{-1}$ :

$$\Phi(\omega) = \alpha g^2 \omega^{-4} \omega_p^{-1} \exp\{-(\omega_p/\omega)^4\} \gamma^\Gamma, \quad (5.1)$$

where

$$\Gamma = \exp\{-(\omega - \omega_p)^2 / 2\sigma^2 \omega_p^2\}.$$

The four parameters of this model are:  $\omega_p$ ,  $\alpha$ ,  $\gamma$ ,  $\sigma$ . We retain the JONSWAP designations:  
 $\omega_p$  is the frequency of the spectral peak;  
 $\alpha$  is the equilibrium range (rear face) parameter;  
 $\gamma$  is the peak enhancement (over the Pierson–Moskowitz spectrum) factor;  
 $\sigma$  is the peak width parameter.

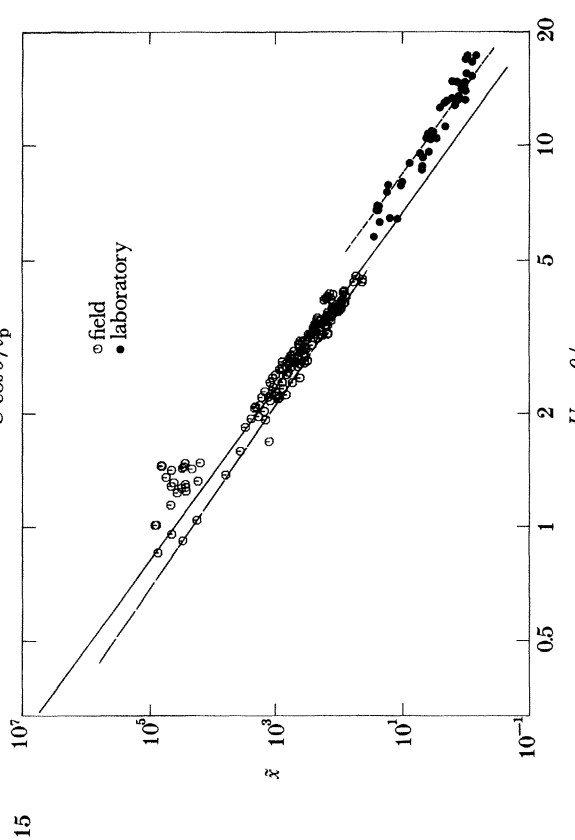
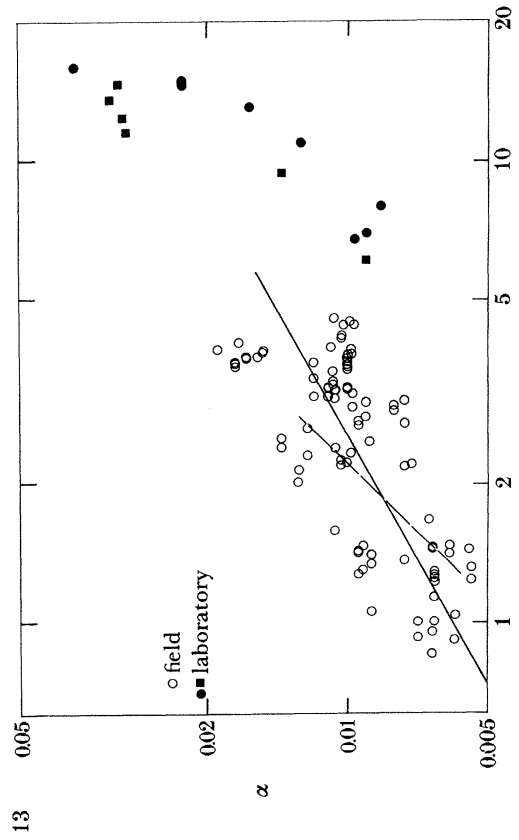
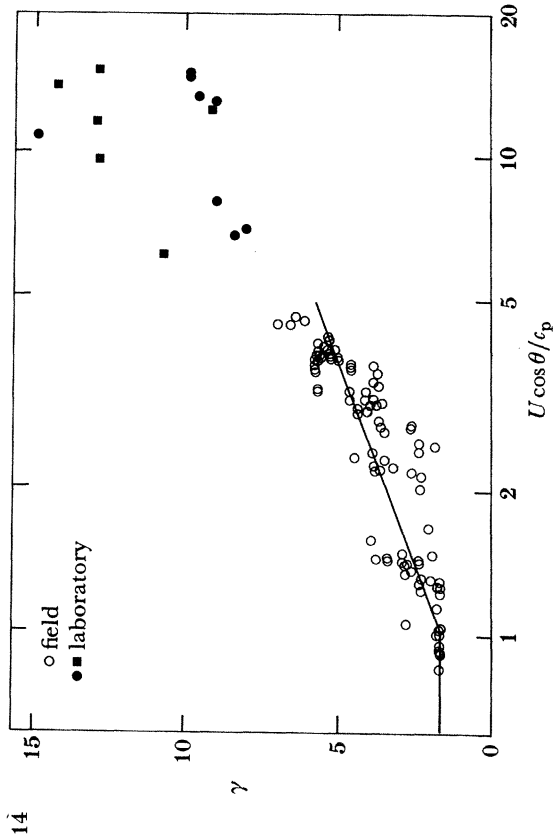


FIGURE 13. The equilibrium range spectral parameter  $\alpha$  against  $U_c / c_p$ . The solid line corresponds to (5.2) and the broken line is from the relation given by Kahma (1981). The data derived from a previous experiment (Donelan 1979) are indicated by solid squares.

FIGURE 14. The peak enhancement parameter  $\gamma$  against  $U_c / c_p$ . The line corresponds to (5.3). The data derived from a previous experiment (Donelan 1979) are indicated by solid squares.

FIGURE 15. Non-dimensional fetch  $\hat{x} = x(\theta) g/(U \cos \theta)^2$  against  $U_c / c_p$ . —: fit to the field data; - - -: fit to the laboratory data; —: from Phillips (1977).

FIGURE 16. Non-dimensional variance of surface elevation  $\tilde{\epsilon} = \epsilon g^2/(U \cos \theta)^4$  against  $U_c / c_p$ . —: fit to the field data; - - -: fit to the laboratory data; the length of the line indicates the range of data gathered during the JONSWAP experiment. Non-dimensional variance of the field data is represented by  $\tilde{\epsilon} = 0.00274 (U \cos \theta / c_0)^{-3.3}$ .

The dependence of the equilibrium range parameter  $\alpha$  on  $U_c/c_p$  is shown in figure 13.  $U_c = U \cos \theta$  is the component of the wind in the direction of travel of the waves at the spectral peak. The ratio  $U_c/c_p$  is a measure of the wind input and might be expected to affect  $\alpha$ . In spite of the scatter in the field observations there is a clear dependence of  $\alpha$  on  $U_c/c_p$ . The field data suggest the following relation between  $\alpha$  and  $U_c/c_p$ :

$$\alpha = 0.006(U \cos \theta/c_p)^{0.55}; \quad 0.83 < U_c/c_p < 5. \quad (5.2)$$

Kahma (1981) argues strongly in favour of an  $\omega^{-4}$  rear face based on accelerometer buoy data from the Gulf of Bothnia. His spectra are based on Toba's (1973) formulation and have an equilibrium range parameter which, converted to the form of  $\alpha$  in (5.1), has the linear wind speed dependence indicated on figure 13 for the range of Kahma's data. Evidently, Kahma's  $\alpha$  is not inconsistent with our data for the range in  $U/c_p$  of his data. However, it cannot be comfortably extrapolated to cover the wider range of our data.

It is also apparent from figure 13 that the laboratory and field data are drawn from different populations. The sudden decrease in  $\alpha$  from the field trend (extrapolated) suggests a basic field-laboratory change in the mechanisms of generation or dissipation of the short waves on the rear face. The most obvious change to the generating process is the constraint on the lateral variation of the wind vector imposed by the tank walls. This would be expected to reduce the directional spread of the 'saturated' waves simply because the mean wind meandering has been arrested. However, there may be an additional reduction in the generation rate, because of the reduced efficiency of mechanisms, such as that hypothesized by Stewart (1974). As the winds are increased, the laboratory waves remain fetch-limited, and the rapid increase of the wind input overcomes the side wall effects;  $\alpha$  increases quickly.

Another possible reason for the initial decrease of the laboratory  $\alpha$  values is the effect of wind drift on limiting the amplitude of the waves at breaking. Banner & Phillips (1974) have shown that the wave amplitudes are reduced by  $(1 - q/c)^2$  where  $q$ , the wind drift, is approximately 0.025  $U$ . For the waves on the rear face at  $\omega = 2\omega_p$ , this reduces to  $(1 - 0.05 U/c_p)^2$ . Initially, this has the effect of reducing  $\alpha$  with increasing  $U/c_p$ . However, eventually the waves become too long for their breaking amplitude to be modified greatly by the thin shear layer at the surface, and the effect of strengthened wind input dominates, which causes  $\alpha$  to increase again.

When the spectra are normalized with respect to the equilibrium range (figure 12), systematic changes in the height of the peak with respect to the parameter  $U_c/c_p$  are manifest. At very low values of  $U_c/c_p$  the peak is actually below the equilibrium range in  $\omega^4 \Phi(\omega)$  coordinates. In the terminology of JONSWAP (Hasselmann *et al.* 1973), the 'peak enhancement parameter'  $\gamma$  is graphed in figure 14. A systematic increase of  $\gamma$  with  $U_c/c_p$  is evident. This contrasts markedly with the JONSWAP result (Hasselmann *et al.* 1973) in which the values of  $\gamma$  derived from individual spectra were scattered over a sixfold range with no significant correlation with non-dimensional fetch. At values of  $U_c/c_p$  less than unity,  $\gamma$  seems to be fairly constant at 1.7. However, the peak value of the spectrum at full development ( $U_c/c_p = 0.83$ ) differs from Pierson & Moskowitz (1964) by less than 20% because the equilibrium range parameter (figure 13) is only 0.0054 at  $U_c/c_p = 0.83$  compared with the constant Pierson-Moskowitz value of 0.0086. For the field data, the peak enhancement factor may be described by:

$$\gamma = \begin{cases} 1.7, & 0.83 < U_c/c_p < 1; \\ 1.7 + 6.0 \lg (U_c/c_p), & 1 \leq U_c/c_p < 5. \end{cases} \quad (5.3)$$

The peak width parameter  $\sigma$  was determined by requiring that the integral under the spectrum (5.1) agree with  $\bar{\zeta}^2$  from (5.7). Agreement within 4% is achieved with:

$$\sigma = 0.08[1 + 4/(U \cos \theta/c_p)^3]; \quad 0.83 < U_c/c_p < 5. \quad (5.4)$$

#### 5.4. Non-dimensional fetch and energy

Figure 15 shows the dependence of non-dimensional fetch  $\tilde{x}$  ( $= x(\theta)g/U_c^2$ ) on  $U_c/c_p$  over five orders of magnitude in  $\tilde{x}$ . Fetch  $x(\theta)$  is the fetch in the direction of propagation of the waves at the spectral peak. Field and laboratory data are nearly contiguous, but a power law (solid line) fitted to the field data clearly does not represent the laboratory results. The laboratory data fall on a line (dotted) which is displaced upward and to the right of the power law representing the field data. Phillips (1977) has remarked that the laboratory and field data summarized by Hasselmann *et al.* (1973) do not necessarily conform to the same similarity law, and he fitted a power law (shown dashed) to their field data only. The laboratory wind speeds are the equivalent neutral profile wind speeds at 10 m height computed with the measured friction velocities. Had we used the wind speed at a lower height, commensurate with the shorter wavelengths of the laboratory waves, the laboratory points would have been in closer agreement with the extrapolated field line of figure 15. However, the opposite trend would have occurred in figure 16, thereby demonstrating that no wavelength-related choice of  $U(z)$  can reconcile the laboratory and field data in terms of Kitaigorodskii's (1962) theory.

For the field data the empirical relation linking non-dimensional fetch and  $U_c/c_p$  is:

$$U \cos \theta/c_p = 11.6\tilde{x}^{-0.23}. \quad (5.5)$$

The change in spectral energy density following the waves is described by the radiative transfer equation (Hasselmann *et al.* 1973):

$$\partial\Phi/\partial t + \bar{v}_i \partial\Phi/\partial x_i = I + W + D, \quad i = 1, 2, \quad (5.6)$$

where  $\bar{v}_i$  is the group velocity averaged over direction, and the right side consists of three sources: wind input  $I$ , wave-wave interaction  $W$ , and dissipation  $D$ .

For the conditions of their fetch-limited data Hasselmann *et al.* (1973) estimate that near the peak the sources are dominated by wind input and wave-wave interaction; dissipation is important only at higher frequencies. However, in the much steeper laboratory data it seems unlikely that dissipation near the peak can be considered negligible. In fact, at high values of  $U/c_p$  visual observation suggests that the waves near the peak of the spectrum are being dissipated by wave breaking. Evidently, the wave-wave interaction processes are too weak to transport the rapid wind input to lower frequencies; there is a pile up of energy near the peak, and the dissipation is increased there. The net effect is that the peak frequency is higher than it would be if wind input and wave-wave interaction dominated the source function. Higher frequency, or lower phase speed  $c_p$ , has the effect of moving the laboratory points to the right in figures 15 and 16.

Figure 16 relates non-dimensional variance  $\tilde{\epsilon}$  ( $= \bar{\zeta}^2 g^2/U_c^4$ ) to  $U_c/c_p$ . The field data seem to be in excellent agreement with a power law dependence (solid line) on  $U_c/c_p$ . Here again the laboratory data deviate from the line, but the disagreement with the field data occurs at somewhat higher values of  $U_c/c_p$  than in figure 15. The non-dimensional variance of the field data is represented by:

$$\tilde{\epsilon} = 0.00274(U \cos \theta/c_p)^{-3.3}. \quad (5.7)$$

In figure 16 we have indicated the range of  $U/c_p$  covered by the JONSWAP data (Hasselmann *et al.* 1973). Over this range their data is sufficiently scattered to cover the solid lines suggested by our data in both figures 15 and 16. In other words, the results of both sets of observations (JONSWAP and this work) are consistent. However, the lines fitted by Hasselmann *et al.* to the JONSWAP data appear to have been biased away from those fitted to our data by the inclusion of laboratory data in the same similarity framework.

### 5.5. Comparison with other spectra

In figure 17 we compare the JONSWAP (Hasselmann *et al.* 1973) and Pierson–Moskowitz (1964) spectra with the spectra represented by (5.1). Two values of  $U/c_p$  (4 and 0.83) are shown which correspond to non-dimensional fetches of  $10^2$  (fetch-limited) and  $10^5$  (fully developed).

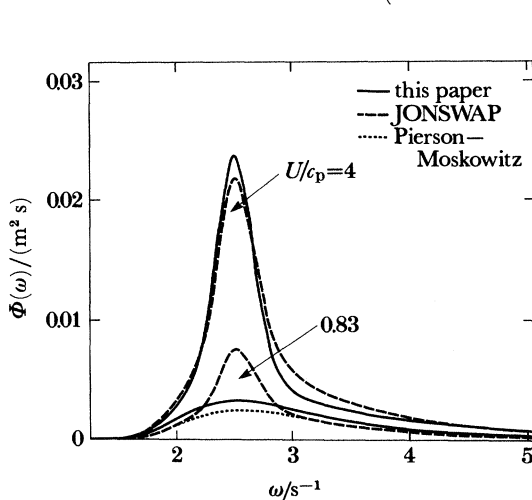


FIGURE 17. Comparison of spectra with  $\omega_p = 2.5 \text{ s}^{-1}$  for two values of  $U/c_p$ .

The values of wind speed and fetch appropriate to these spectra ( $\omega_p = 2.5 \text{ s}^{-1}$ ) are respectively  $15.6 \text{ m s}^{-1}$  and  $2.5 \text{ km}$  (fetch-limited) and  $3.2 \text{ m s}^{-1}$  and  $104 \text{ km}$  (fully developed). The Pierson–Moskowitz spectrum applies only to full development, and it is encouraging that the spectrum of (5.1), derived from fetch-limited data only and extrapolated to full development, is in good agreement with the Pierson–Moskowitz. At the other end of the scale of strongly fetch-limited spectra, the JONSWAP spectrum is in reasonable agreement with (5.1). However, the JONSWAP spectrum, extrapolated to full development, retains its enhanced peak and is therefore unable to relax to the broader peaked fully developed spectrum. The differences between the JONSWAP spectrum and (5.1) hinge on the choice of the power law for the rear face of the spectrum. Figure 12 amply establishes the choice of  $\omega^{-4}$  for these data, and the much-reduced scatter in  $\alpha$  and  $\gamma$  relative to the JONSWAP results, coupled with the smoother transition from fetch-limited to fully developed conditions, attests to the appropriateness of the spectral description of (5.1).

### 6. WAVE DIRECTION AGAINST WIND DIRECTION

Both in the execution of steady-state fetch-limited experiments and in the application of fetch-limited formulae in hindcasting, it is common practice to assume that the mean wave propagation direction agrees with the wind direction. That this cannot be true in general is

evident from the fact that waves are not strictly locally generated, but instead are the net result of their development along the entire upwind fetch. If, therefore, the gradient of fetch about the wind direction is large, one might reasonably expect the wave direction to be biased towards long fetch, where the reduced generating force of the lower wind component ( $U \cos \theta$ ) is more than balanced by the longer fetch over which it acts. In figure 18 the observed mean direction of the waves near the peak of the spectrum is plotted against average wind direction. The straight line (dashed) is the line of perfect agreement with the wind direction. When the fetch gradient is small – wind directly offshore ( $-120^\circ$ ) or along the long axis of the lake ( $75^\circ$ ) – the wave and wind directions agree. Otherwise, the discrepancies can be as much as  $50^\circ$ . Certainly such differences call into question the validity of hindcasting techniques which disregard them.

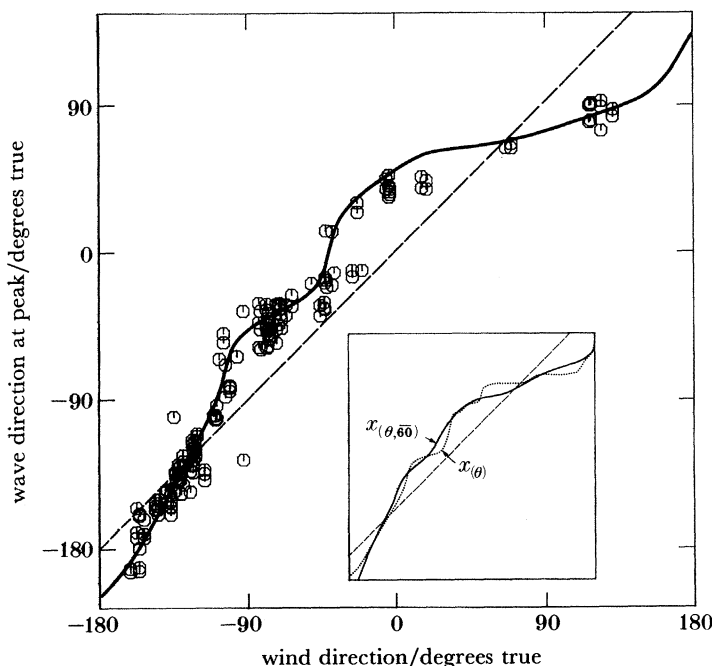


FIGURE 18. Mean direction of waves at the spectral peak against mean wind direction (approach bearing in both cases). The broken line is the line of perfect agreement; the solid line has been deduced from similarity considerations (6.1), with fetch averaged over  $30^\circ$  ( $\pm 15^\circ$ ) about the wave approach direction. The inset demonstrates the relative insensitivity to choice of averaging over  $60^\circ$  (solid) or not at all (broken).

Initial attempts to use Kitaigorodskii's scaling law for non-dimensional frequency with fetch in the wind direction produced a much poorer correlation than that of figure 15. This supports the view that, unless the wind is blowing directly offshore from a straight shoreline, more appropriate parameters for similarity scaling are the fetch and wind component in the wave direction rather than the wind direction. The similarity relation of (5.5) may be written in terms of the peak period  $T_p$ :

$$T_p = 0.54 g^{-0.77} U^{0.54} (\cos \theta)^{0.54} x^{0.23}, \quad (6.1)$$

where  $x$  is the fetch in the wave propagation direction.

Since the energy density at the peak of the spectrum is roughly proportional to  $T_p^5$  (Phillips 1977, figure 4.8), it is clear that the direction  $\theta$  which yields the largest value of  $T_p$  from (6.1) will be the direction of approach of the waves at the peak of the spectrum.

For any wind speed  $U$  such that the waves are fetch-limited, the right side of (6.1) ( $\cos \theta x^{0.426}$ ) may be maximized to yield the offwind angle of approach of the peak of the spectrum  $\theta$ . Running averages of the geometric fetch at increments of  $1^\circ$  over various windows from  $\pm 0^\circ$  to  $\pm 30^\circ$  were computed and used to deduce the approach direction of the peak wave. The sensitivity to width of averaging window was not large, as demonstrated in the inset to figure 18 for window widths of  $0^\circ$  and  $60^\circ$ . The best agreement (solid line in figure 18) with the observed wave approach direction was achieved with window width of  $30^\circ$ , i.e.  $\pm 15^\circ$  on either side of  $\theta$ .

## 7. PHASE SPEED

### 7.1. Introduction

Attempts to assess the behaviour of natural waves by using laboratory tanks often run into some difficulty with the excess of steepness of laboratory tank waves over natural waves. This comes about because strong wind forcing is necessary to produce a reasonable spectrum of gravity waves in the short fetches (under 30 m) possible in most laboratory tanks. The presence of harmonics can be seen in the power spectra, and the dispersion relation (figure 19) is typically as described by Ramamonjiarisoa (1974). Spectra of natural wind waves, on the other hand, do not show pronounced harmonic peaks. In this regard, we were able to employ the longer fetch possible with our tank to produce waves which were reasonable facsimiles of natural waves. Compare the double logarithmic frequency spectra of figure 20 and the dispersion relation of figure 19 for the natural waves of run 128173 ( $U_c/c_p = 3.6$ ) with those of the laboratory run 3 ( $U/c_p = 8.5$ ). On the basis of these two figures only, one would be inclined to group laboratory run 3 with the natural waves rather than with the steeper laboratory waves of runs 5, 7 and 30 ( $U/c_p = 11.8, 15.9$  and  $16.5$ , respectively). It appears that laboratory experiments in large tanks can produce results that are contiguous with observations in nature in some respects, though not all (see §5).

In this section we explore the dispersion relation of waves in the laboratory and in the field. We make use of the greater statistical reliability and accuracy of the laboratory measurements to assess directly the significance of bound harmonics of the steep waves near the peak. In extending these results to the field, we attempt to provide a coherent picture of the dispersion relation for wind-generated waves in field or laboratory.

### 7.2. Average phase speed

Having gained access to the wavenumber-frequency spectrum  $X(\mathbf{k}, \omega)$ , we are able to examine the phase-speed characteristics of wind-generated gravity waves in a direct way. As the phase speed of any frequency component is defined by  $c(\omega) = \omega/k$ , we may examine the average phase speed of any frequency component  $\omega_1$  by obtaining an average wavenumber  $\bar{k}(\omega_1)$  from  $X(\mathbf{k}, \omega_1)$

$$\bar{k}(\omega_1) = \iint k X(\mathbf{k}, \omega_1) dk_x dk_y / \iint X(\mathbf{k}, \omega_1) dk_x dk_y. \quad (7.1)$$

Calculations of the phase speed done in this way are shown in figure 19; they are in ascending order of  $U_c/c_p$ . The lowest two are derived from field data, the rest from laboratory data. The hyperbola (solid line) represents the dispersion relation given by linear theory:  $c = g/\omega$ . At the lowest value of  $U_c/c_p$  the wave field is almost fully developed and the waves at the peak obey

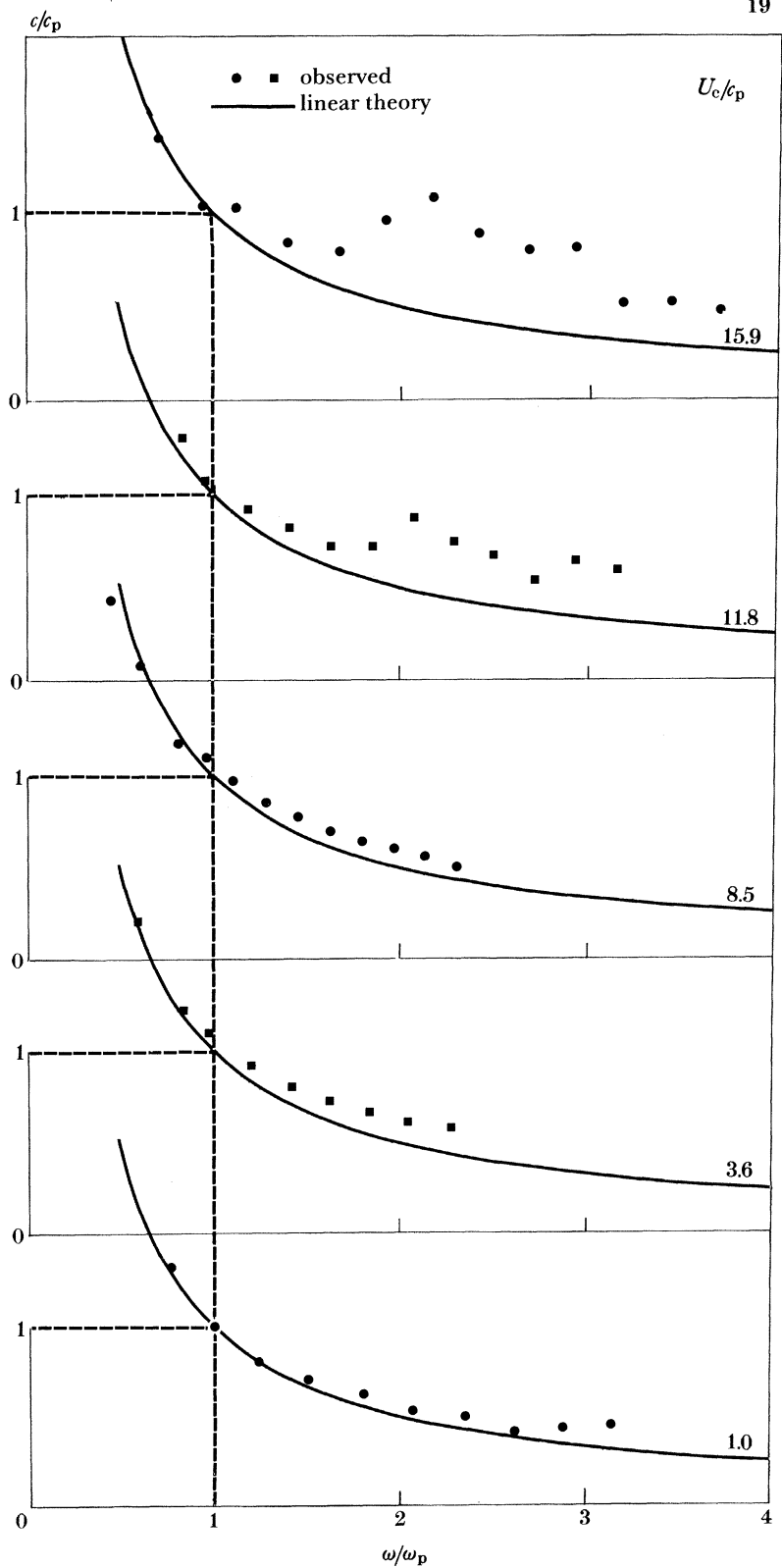
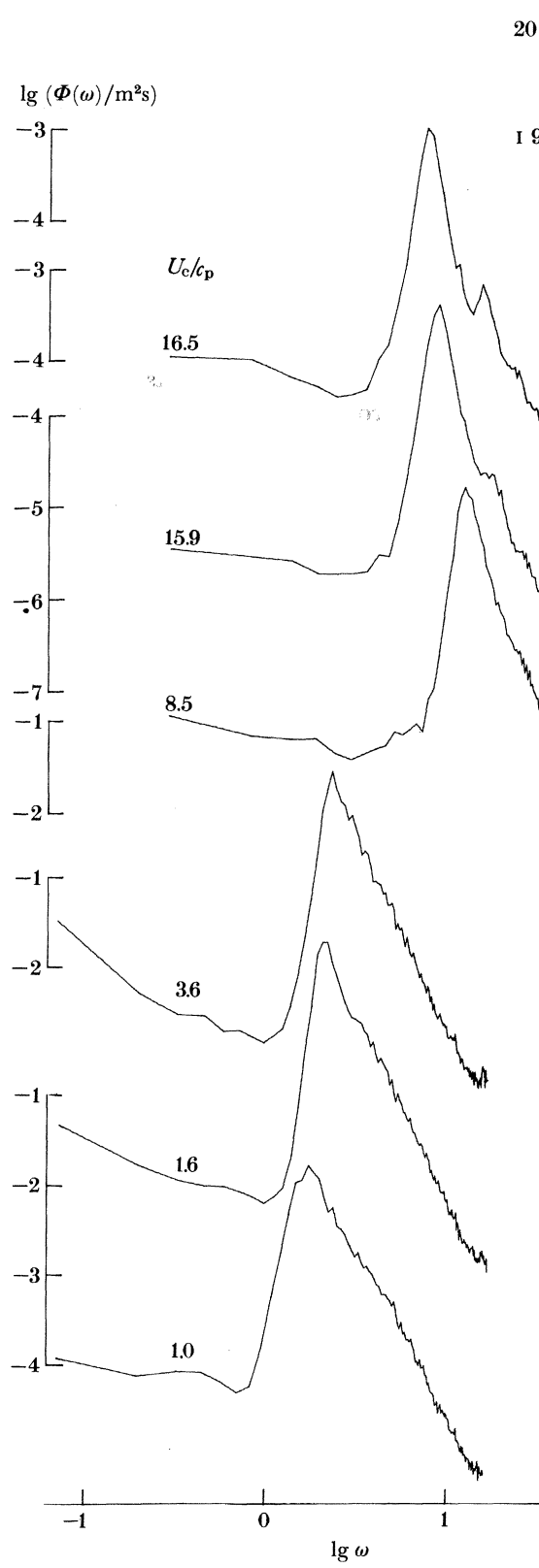


FIGURE 19. Normalized average phase speed against  $\omega/\omega_p$  for five spectra. The two at the bottom of the figure are from field data, the others from laboratory data. As  $U_c/c_p$  increases the effects of bound harmonics are apparent. The normalizer  $c_p$  is the theoretical linear phase speed of the peak waves  $c_p = g/\omega_p$ .

FIGURE 20. Double logarithmic spectra for three runs of field waves (bottom) and three runs of laboratory waves. With increasing  $U_c/c_p$  the spectra become narrower and acquire secondary peaks at  $n\omega_p$ . The 90% confidence limits are indicated by a vertical bar.



the linear dispersion relation. However, at somewhat higher frequencies than at the peak, the measured phase speeds are in excess of the theoretical. In all but the lowest value of  $U_e/c_p$  the measured phase speeds near and above the peak are in excess of the theoretical phase speed. The deviation from the theoretical value increases steadily with  $U_e/c_p$ , until at the highest values of  $U_e/c_p$  the phase speed at twice the peak frequency  $\omega_p$  is about equal to the phase speed at the peak. As already noted in §4.2, this behaviour is due to the presence of bound harmonics as reported previously by Ramamonjarisoa (1974), Lake & Yuen (1978) and Mitsuyasu *et al.* (1979). Plant & Wright (1980), on the other hand, find that their observed deviations from the linear dispersion relation were best accounted for by Doppler shift caused by wind drift.

Komen (1980) has calculated the expected phase speed changes based on a balance of free and bound waves. His results are qualitatively similar to those shown in figure 19.

Apart from the work of Plant & Wright (1980), previous laboratory phase-speed measurements have been based on two-point correlations of surface-intersecting wave gauges. This method of phase-speed measurement can produce misleading results. To quote Phillips (1980), ‘the two-point phase correlation methods suffer from an instrumental bias, a stationary phase bias, which for the short components of the wavefield emphasizes the conditions at the crest of long waves. I believe that these techniques measure not the average speed of the short wave but the speed of these components at the long-wave crest, which is the sum of their propagation speed plus the orbital velocity of the long waves. As we examine higher and higher frequencies, their intrinsic propagation speed becomes a smaller fraction of the orbital velocity of the long wave and one might expect that the measurements would become asymptotic towards the orbital speed at the long-wave crests. This happens both in the laboratory and in the field, but under laboratory conditions the situation is accentuated since the primary waves are very steep, with prominent harmonics.’ Our method is free of these uncertainties since we obtain the full three-dimensional wavenumber–frequency spectrum, from which the average wavenumber in any frequency band, and thus the average phase speed, may be obtained.

In strongly forced laboratory situations as in run 5, the energy observed in the neighbourhood of  $\omega = 2\omega_p, 3\omega_p, 4\omega_p, \dots$  is largely a result of higher harmonics bound to the dominant wave near the peak frequency  $\omega_p$ . (The balance between such bound harmonics and free waves will be explored further in this section.) Thus the second harmonic of the dominant wave  $\omega_p$  would show up in the wavenumber spectrum for frequency  $2\omega_p$  at about<sup>†</sup> half of the radius of the linear dispersion circle, whereas the third harmonic would show up in the wavenumber spectrum for frequency  $3\omega_p$  but at about a third of the radius of the circle, etc. For the bound harmonics the phase speed at  $\omega = 2\omega_p, 3\omega_p, \dots$  is the same as that at the peak  $c_p$ . However, as the spectrum is not a delta spike at  $\omega_p$ , but rather a narrow spectrum with most of the energy concentrated in a frequency band  $\Delta\omega$  around  $\omega_p$ , the effects of higher harmonics of the components in this frequency band will lead us to the conclusion that the phase speed must be almost equal to  $c_p$  in the frequency bands  $2\Delta\omega$  around  $2\omega_p$ ,  $3\Delta\omega$  around  $3\omega_p, \dots$ , etc. All these theoretical predictions are indeed observed experimentally for high values of  $U/c_p$ . While this explanation is similar to those offered by Phillips (1977), it should be pointed out that his explanation is not valid for frequencies between  $\omega_p$  and  $2\omega_p - \Delta\omega$ , and between  $2\omega_p + \Delta\omega$  and  $3\omega_p - \frac{3}{2}\Delta\omega$ , etc. For these frequencies, the departure from the dispersion circle must be a result

<sup>†</sup> More precisely the bound energy in the  $n$ th harmonic would appear at  $1/n$  the radius of the nonlinear dispersion circle corresponding to (1.3) since the harmonics travel at the speed of their fundamental which itself, by virtue of the existence of harmonics, is in agreement with (1.3) rather than with (1.1).

of the local effects of finite wave slope (as discussed in §1) which can be up to about 20% in wavenumber or 10% in phase speed, in agreement with observations (figure 19). By combining both effects of higher harmonics and of the local Stokes effect, theory predicts that the curve of average phase speed against frequency for  $\omega > \omega_p$  is wavy, but as  $\omega$  increases will tend to a relatively constant level near  $c_p$  if the bound harmonics contain much more energy than the free waves at these frequencies. This occurs when  $\omega/\omega_p \geq \omega_p/\Delta\omega - \frac{1}{2}$  in strongly forced cases and is clearly confirmed by laboratory experiments for large values of  $U/c_p$  (figure 19).

For historical perspective we have opened this section with a look at average phase speeds. Observations of phase speeds in both natural and laboratory conditions have given rise to questions regarding the dispersive nature of wind waves. Should we regard the wave field at  $\omega > 1.5 \omega_p$  as non-dispersive on the basis of observations such as those reported above? Observations of average phase speeds are somewhat ambiguous because, if bound waves do exist, averages over the wavenumber plane or two-point correlations include the effect of two dynamically quite distinct sets of waves. Fortunately in our case we can, in principle, restrict our attention to regions of the wavenumber plane that contain only free waves or any of the several bound harmonics.

### 7.3. Phase speed of free waves

In figure 21 we examine the phase speed of the free waves only. This is done by obtaining an average wavenumber over a band of wavenumbers limited at low wavenumber by the arithmetic mean of the expected free wavenumber ( $k_f = \omega^2/g$ ) and the expected second harmonic wavenumber ( $k_2 = \omega^2/2g$ ) and limited at high wavenumber by a band of equal width. The effects of amplitude dispersion are now clear. The almost fully developed case ( $U_c/c_p = 1.0$ ) shows no sign of amplitude dispersion below  $\omega/\omega_p = 1.3$ . Above this there is a moderate increase in the phase speed above the theoretical curve. With increasing  $U_c/c_p$  the effects of amplitude dispersion are noticeable near the peak and above. On the assumption that the waves are distorted in accordance with the Stokes theory† (§1), the maximum amplitude dispersion corresponding to the Stokes steepness limit ( $ak = 0.44$ ) is 10%. At the highest values of  $U_c/c_p$  the waves at frequencies just above the peak approach the phase speed appropriate to the maximally steep Stokes waves. It is interesting to note that at the highest value of  $U_c/c_p$  the phase speed near the peak shows less evidence of amplitude dispersion than in the laboratory runs at somewhat lower  $U_c/c_p$ . It is possible that widespread breaking of the waves near the peak reduces the steepness of these waves. This interpretation is consistent with the calculations of Longuet-Higgins & Cokelet (1976) which show that waves reach their maximum steepness and speed somewhat before breaking.

### 7.4. Phase speed of bound harmonics

One can also determine the dispersion relation of the bound harmonics. To avoid contamination of the average wavenumber of the second harmonic, the region in wavenumber space considered was bounded below by the arithmetic mean of the expected wavenumber of the second and third harmonics ( $k_n = \omega^2/ng$ ), and above by the arithmetic mean of the expected wavenumber of the second harmonic and of the free wave at that frequency. It was possible to resolve the average wavenumber for the second harmonic in the laboratory runs with high

† Support for this is provided by Lake & Yuen (1978) who have shown good agreement between the ratio of spectral amplitudes of harmonic and fundamental and the predictions of the Stokes (1847) theory.

## DIRECTIONAL SPECTRA OF WIND WAVES

545

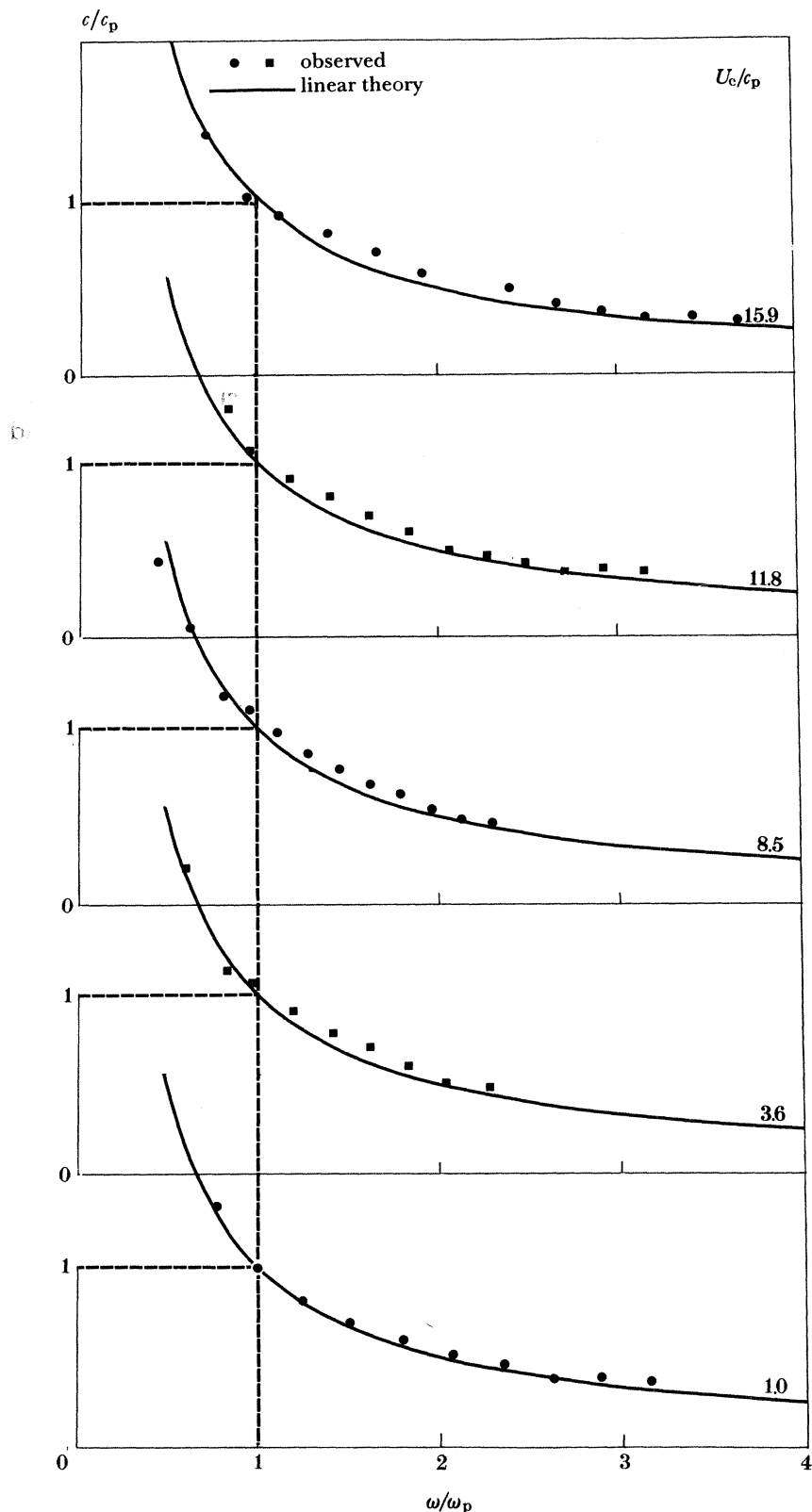


FIGURE 21. Normalized phase speed of free waves for the same five spectra as in figure 19. The effects of amplitude dispersion with increasing  $U_e/c_p$  are apparent.

values of  $U/c_p$  only. These are shown in figure 22. The lower hyperbola is, as before, the theoretical linear dispersion relation; the upper hyperbola is the locus of speeds twice as great as the lower and is the speed at which bound second harmonics would travel if trapped on waves of half the frequency on the lower curve. The bars correspond to limits of the band of averaging, and the dashed line is what would result from a uniform distribution of energy within

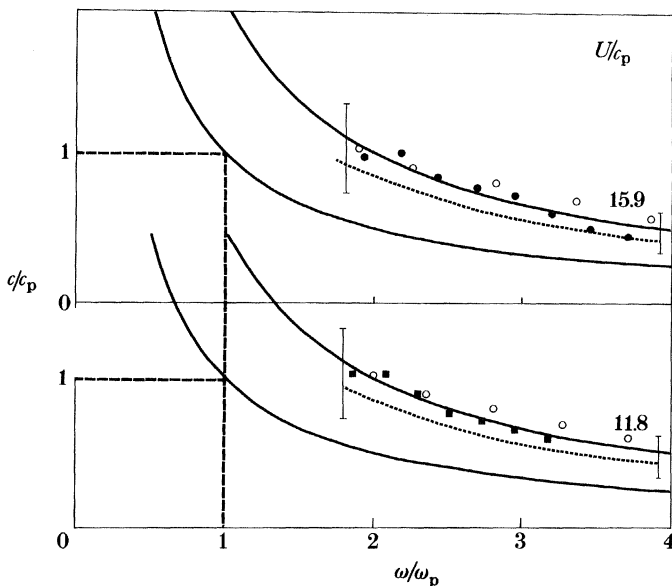


FIGURE 22. Normalized phase speed of the bound second harmonic for the two highest  $U/c_p$  cases. The solid symbols are the measured values; the open circles are taken from figure 21 transposed to twice the frequency, and represent the expected speed of second harmonics bound to the observed peak waves.

the band; i.e. white noise. At frequencies below 2.0 Hz we cannot separate effectively second and third harmonic contributions to the energy density. Lower frequencies do not, therefore, appear in figure 22. At the highest frequencies the points approach the white noise result. Between these two extremes, however, the phase speeds very definitely support the idea that these are second harmonics of the free waves of figure 21. The open circles are taken from the measured phase speeds of figure 21 transposed to twice the frequency. They represent the speed at which the bound harmonics must travel to be consistent with the measurements of figure 21. While it is possible that wind drift could affect the measured phase speed, it will not affect the comparison between figures 21 and 22 discussed above.

### 7.5. Amplitude dispersion and Doppler shift of laboratory waves

It is, of course, impossible to generate wind waves without also producing a strongly sheared current near the surface. The presence of such a current has been used by some researchers (Lake & Yuen 1978; Mitsuyasu *et al.* 1979; Plant & Wright 1980) to explain part of the excess speed of measured waves above the linear theory. In addition, Plant & Wright (1980) have pointed out that the wind itself will change the propagation speed of the waves a small but measurable amount. We recognize that some effect of both current and wind forcing must be present in our data. However, since our laboratory waves are somewhat longer than those discussed in previous work, yet our wind speeds and currents are similar, these effects would be less pronounced in our data. None the less, in the following we assess the effects of currents.

The ratio of the energy in the bound wave to the free wave is graphed against  $\omega/\omega_p$  in figure 23 for the laboratory data. It is clear that with increasing  $U/c_p$  the energy in the second harmonic waves begins to dominate the spectrum above  $\omega/\omega_p = 1.9$  and the shape of the peak of the spectrum – forward face sharper than rear – is reflected in the energy of the second harmonic. It would seem that at values of  $U/c_p$  in excess of 9, evidence for bound harmonics will appear in the power spectra and the dispersion relation at values of  $\omega/\omega_p$  in the neighbourhood of 2.1. Such values of  $U/c_p$  occur only fleetingly in nature except on small ponds. Thus the theoretical dispersion relation with some amplitude dispersion is generally adequate to describe natural wind-generated wave spectra and laboratory tank spectra for which  $U/c_p < 9$ .

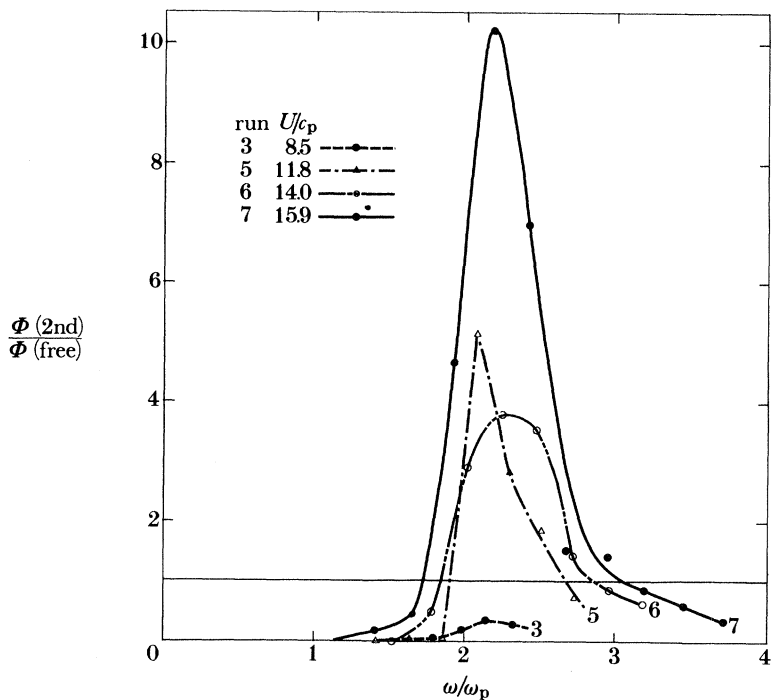


FIGURE 23. The balance of energy in bound second harmonics to free waves at the same frequency. Somewhere in the range  $8.5 < U/c_p < 11.8$  the energy in the second harmonic of the peak first exceeds the energy in the free waves at  $\omega = 2\omega_p$ .

We now turn our attention to the question of how much amplitude dispersion is appropriate. As we have access to the energy in the bound harmonics, we may compare this with the energy in the corresponding free wave (fundamental) and, in a Stokian model (1.2), thereby establish the slope of the fundamental wave. Figure 24 shows the result of this calculation for the laboratory data. The steepness increases steadily above the peak and begins to approach the theoretical limit at  $\omega/\omega_p = 1.5$ . Beyond this there is insufficient resolution of the wavenumber spectra to determine the energy in the second harmonic which would be found at  $\omega/\omega_p > 3.0$ . We know that the spectrum falls off to infinitesimal amplitudes at  $0.6 < \omega/\omega_p < 0.8$  (see figure 11) so that the extrapolation towards low  $\omega/\omega_p$  values is probably in order.

These steepness estimates allow us to compute the Stokes phase speeds for the free waves (3.1) and to compare them with the observed phase speeds of figure 21. The difference (measured phase speed  $c_m$  minus the Stokes phase speed  $c_s = g/\omega[1 + (ak)^2 + \frac{5}{4}(ak)^4]^{\frac{1}{2}}$ ) is further adjusted

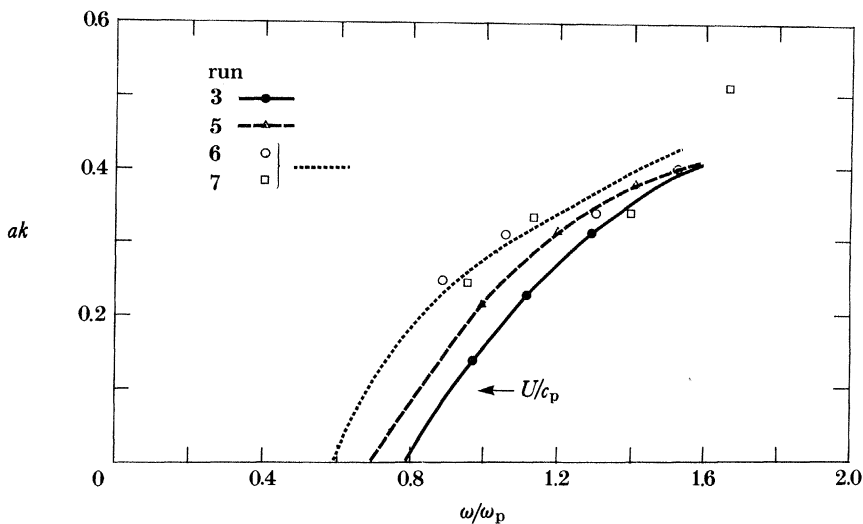


FIGURE 24. The steepness of spectral components of laboratory waves deduced from the balance of energy in second harmonics to that in the fundamental components.

by the correction given by Plant & Wright (1980) to account for the air flow over the waves  $c_a$ . The Stokes correction is positive and can account for up to 10% of the linear theory; the air flow adjustment  $c_a$  is negative and between 1 and 3% in all cases. The difference  $(c_m - c_s - c_a)$  varies between -4 and +10% and probably consists of a combination of experimental error and differential advection of the wave components by sheared current.

In the laboratory tank the wind-driven current profile has been found to scale with the surface friction velocity and the total depth (Donelan 1978). In figure 25, therefore, we examine the difference  $(c_m - c_s - c_a)_k$  normalized by the surface friction velocity in the water  $u_*$  against the

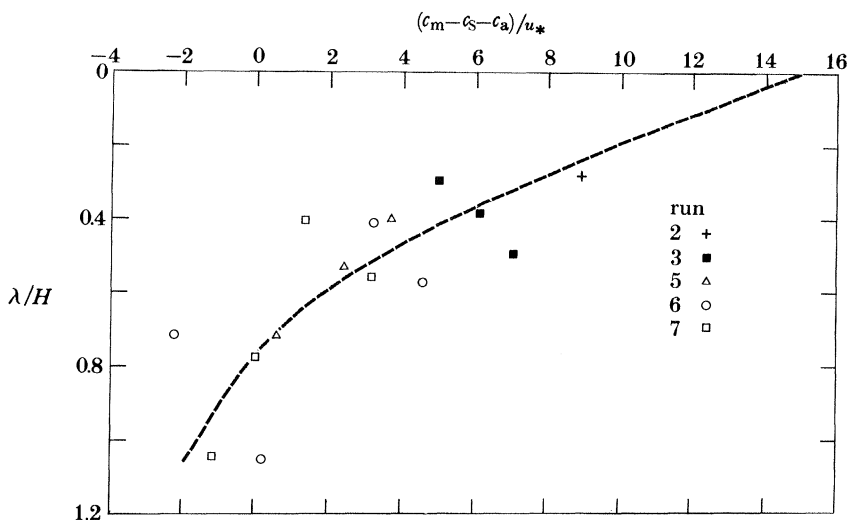


FIGURE 25. Measured phase speed minus amplitude dispersion minus wind forcing. This residual normalized by the friction velocity in the water  $(\tau/\rho_w)^{1/2}$  shows a depth dependence similar to the velocity profile measured by Donelan (1978) under similar conditions in the same tank. This similarity is exploited to deduce that the waves are being advected by the wind drift at a speed commensurate with the current at depth  $z$  such that  $kz = 1$ .

wavelength  $\lambda (= 2\pi/k)$  to total depth  $H$  ratio. Although the data are somewhat scattered, there is a definite trend from slow upwind advection of the longer wavelengths  $\lambda/H > 0.8$  to downwind advection of the shorter wavelengths, which when extrapolated to vanishing wavelengths suggests a surface advection of  $15u_* \approx 0.02U$ . Calculations by Stewart & Joy (1974) suggest that the waves are advected by the mean current at a depth corresponding to some fraction of a wavelength depending on the current profile. From matching the wind-driven current profile obtained by Donelan (1978) from the same tank as in the present experiment, it would appear that the current at depth  $z = 1/k$  is reflected in the residual wave advection speed after amplitude dispersion and wind forcing have been accounted for.

### 7.6. Amplitude dispersion of field waves

We are unable to compute the Stokes distortion from the relative magnitudes of free waves and harmonics because of lack of sufficient resolution at high frequencies in the field directional spectra. Instead, having gained confidence from the consistent picture provided by the laboratory results, we shall do the calculations in reverse order for the field data. That is, having first removed the calculated effects of wind forcing  $c_a$  ( $0.28/k$ ) and drift current  $U_w$  ( $-1/k$ ), the residual measured phase speed excess will be taken to be due to amplitude dispersion and will be used to estimate the slope (figure 26). The drift current profile scaled by the friction velocity is computed based on the field measurements by Donelan (1978) at the same site. Figure 26 and table 2 are summaries of the 18 field cases in which the directional spectra were well resolved to at least  $\omega/\omega_p = 2.2$ . They are grouped by  $U_c/c_p$ . The two higher  $U_c/c_p$  curves show a consistent picture of appreciably steep waves in the region near the peak ( $0.9 < \omega/\omega_p < 2.0$ ). For the lower  $U_c/c_p$  case the steepness rises to nearly 0.3; in the other case ( $U_c/c_p = 2.9$ ) the steepness rises to nearly 0.4.

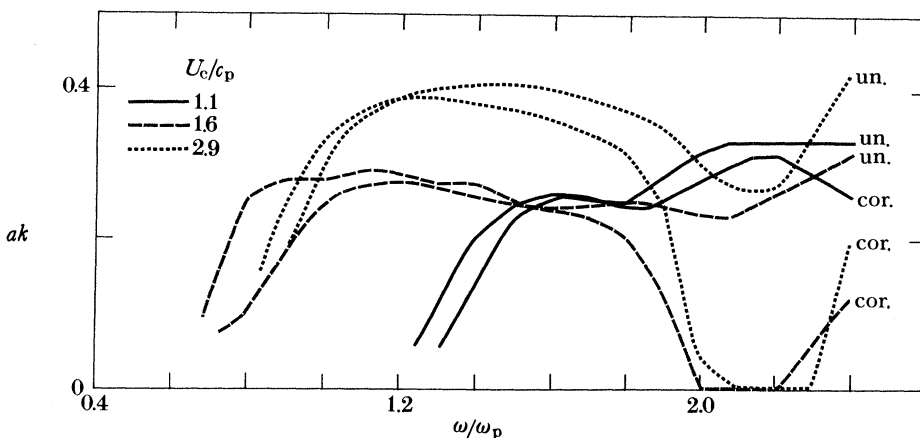


FIGURE 26. Wave slope deduced from measured phase speeds by using (1.3). Eighteen field cases have been grouped into three sets by  $U_c/c_p$ . A pair of curves in each set corresponds to slopes computed from the uncorrected (un) and corrected (cor) phase speeds. The differences between corrected and uncorrected are larger for the high  $U_c/c_p$  cases since these correspond to strong winds and short waves.

Figure 26 shows the steepness both with and without correction for the assumed drift current and wind forcing. In the steady state these effects are proportional to  $u_*$ . The almost fully developed case with small  $u_*$  is hardly affected by these corrections. On the other hand, the

TABLE 2. R.M.S. SLOPES OF FIELD DATA

year	run	$U/\text{m s}^{-1}$	$\omega_p/\text{rad s}^{-1}$	$\bar{\zeta}^2/\text{cm}^2$	$U_c/c_p$	significant slope (%)	r.m.s. slope
1976	305093	7.2	2.13	173	1.57	0.97	0.061
	305094	7.1	1.99	161	1.45	0.82	0.051
	339063	7.2	2.20	216	1.61	1.15	0.073
	339064	7.6	2.13	222	1.65	1.10	0.069
	342163	8.6	2.27	126	1.97	0.94	0.059
	342164	8.7	2.27	130	1.70	0.95	0.060
	356123	11.6	2.15	368	2.52	1.44	0.090
	356124	11.5	2.09	379	2.44	1.38	0.087
	362053	6.0	1.77	165	1.08	0.65	0.041
	362054	5.7	1.78	142	1.03	0.61	0.038
1977	006003	5.7	2.32	87	1.34	0.81	0.051
	006004	5.5	2.32	80	1.29	0.78	0.049
	119013	6.7	2.26	91	1.55	0.79	0.050
	119014	7.0	2.26	102	1.61	0.84	0.053
	128173	15.4	2.27	220	3.55	1.24	0.078
	128174	15.2	2.31	213	3.61	1.26	0.079
	128203	13.3	1.95	281	2.64	1.03	0.065
	128204	12.7	2.15	294	2.76	1.29	0.081

moderately generated case has its phase speed excess and concomitant steepness reduced to zero near  $\omega/\omega_p = 2.1$ , while the strongly generated case with large  $u_*$  appears to be overcorrected. Quite possibly the drift currents have been overestimated. It may be that the steady-state profile assumed for the drift current is in error. The spin up time for the Ekman boundary layer is of the order of half a pendulum day or about 17 h for Lake Ontario, which is generally longer than the duration of the wind system before the wave measurements. The matter cannot be resolved without coincident wave and current profile measurements, but it seems probable that the correct values lie between the corrected and uncorrected curves for each  $U_c/c_p$  in figure 26. In any case, near the spectral peak  $0.8 < \omega/\omega_p < 1.6$ , the estimates of  $ak$  are not greatly affected by the drift current. Here we find that the moderately and strongly developed cases are more or less uniformly steep, while the nearly fully developed case reaches its maximum steepness at about twice the peak frequency.

The lowest value of  $U_c/c_p$  ( $= 1.1$ ) represents nearly fully developed waves. The steepness at the peak, where there is very little direct wind input and wave-wave interaction effects are not strong in this case (Dungey & Hui 1979), is negligible. However, at  $\omega/\omega_p \approx 2.2$  the steepness increases to a value somewhere between the maxima of the other two curves. Evidently, near full development the wind input at frequencies somewhat above the peak is relatively large compared with that of the peak. Figure 26 suggests that, except for the nearly fully developed case, the steepness drops off markedly above  $\omega = 1.8 \omega_p$ . This is consistent with the idea of peak enhancement (figure 12) in which the spectral levels at a particular frequency can be largest when that frequency is the peak frequency. This may occur when the peak enhancement factor  $\gamma$  exceeds  $e \doteq 2.7$ . The values of  $\gamma$  corresponding to the three curves of figure 26 are, in order of increasing  $U_c/c_p$ , 1.9, 2.9 and 4.5.

## 8. DIRECTIONAL DISTRIBUTIONS OF WAVE ENERGY

8.1. *Introduction*

In this section we shall concern ourselves entirely with the description of natural (field) directional spectra. Two examples of the two-dimensional directional spectrum (defined by (3.4)) are shown in figures 27 and 28 for quite different values of  $U_e/c_p$ : 1.5 and 3.1, respectively. These are derived from the wavenumber spectra of figures 8 and 9 respectively in the manner described in §3.4. The ordinates are not in relative scale but the frequency spectrum  $\Phi(\omega)$  is shown in figures 8 and 9. A measure of the level of confidence of the polar spectrum is given by the dashed line.

The polar spectra are predominantly unimodal and tend to be more or less symmetrical about their peaks. The most obvious features are the difference between wave propagation direction and wind direction near the peak, and the directional broadening with increasing frequency above the peak. The first has been discussed in §6, and figures 27 and 28 demonstrate that with increasing frequency the mean wave direction becomes more and more closely aligned with the wind: a reflection of the short relaxation time of the short waves and hence their insensitivity to the distant fetch distribution. The second has been noticed by previous authors (Longuet-Higgins *et al.* 1963; Hasselmann *et al.* 1973; Mitsuyasu *et al.* 1975; Hasselmann *et al.* 1980) and attempts have been made to parameterize the spreading function in various ways. Currently, perhaps because most published directional spectra have been obtained from pitch-roll buoys, the most popular parametric description is based on the  $\cos^{2s}(\frac{1}{2}\theta)$  form first suggested by Longuet-Higgins *et al.* (1963). Unfortunately, attempts to tie down the behaviour of the  $s$  parameter have led to disagreement rather than consensus, in spite of the fact that the best known attempts to parameterize  $s$  have all been based on floating buoys. In the following we shall explore the behaviour of  $s$  and compare our results with previous work. Finding that  $\cos^{2s}(\frac{1}{2}\theta)$  does not describe our results adequately we shall propose another description.

8.2. *The s parameter*

Mitsuyasu *et al.* (1975) were the first to present a reasonably comprehensive set of estimates for  $s$  using measurements obtained from a cloverleaf buoy. They presented a plot of  $s$  against  $U/c$  and showed that although there was good clustering for points on the rear face of the spectrum the points on the front face did not cluster.

Subsequently, Hasselmann *et al.* (1980) using measurements made from a pitch-roll buoy confirmed this behaviour, but also showed that, when plotted against the relative frequency, the front face ( $\omega/\omega_p < 1$ ) could also be made to cluster. This result, that the width distribution of the spectrum is apparently independent of the wind strength, was attributed by Hasselmann *et al.* to the dominance of wave-wave interaction over wave-generation effects, a point that we shall discuss further in §8.4.

Their estimates for  $s_1$  were obtained by using the first two Fourier coefficients for  $F(\omega_n, \theta)$  as follows

$$\pi F(\omega_n, \theta) = (\frac{1}{2} + a_1 \cos \theta + b_1 \sin \theta) \Phi(\omega_n), \quad (8.1)$$

$$r_1 = (a_1^2 + b_1^2)^{\frac{1}{2}}, \quad (8.2)$$

$$s_1 = r_1 / (1 - r_1). \quad (8.3)$$

28

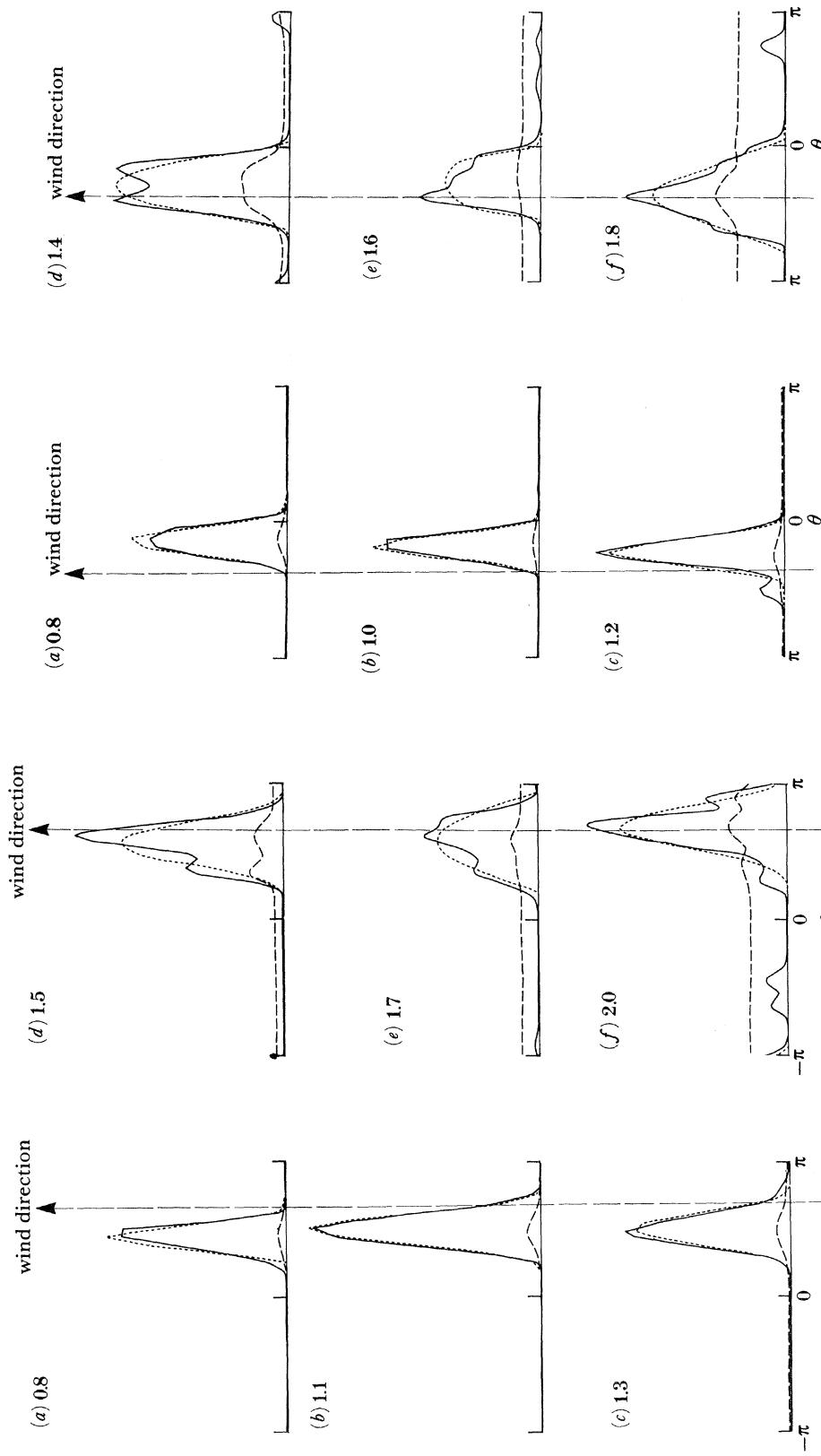


FIGURE 27. Directional (or polar) spectra  $F(\omega, \theta)$ , (3.4) corresponding to the wavenumber spectra of figure 8. The solid line is the parametric representation described in § 3.4; the dashed line is a measure of the error in the estimation of  $F$ .  $U \cos \theta/c_p = 1.5$ ;  $\omega_p = 2.13 \text{ s}^{-1}$ ; and values of  $\omega/\omega_p$  are stated on the figure.

27

FIGURE 28. Directional spectra corresponding to the wavenumber spectra of figure 9.  $U \cos \theta/c_p = 3.1$ ;  $\omega_p = 2.31 \text{ s}^{-1}$ , and values of  $\omega/\omega_p$  are stated.

The Fourier coefficients  $a_1$  and  $b_1$  were obtained from the spectrum of the two orthogonal wave slopes or surface horizontal accelerations. For narrow distributions ( $r_1 \approx 1$ ),  $s_1$  is very sensitive to the width.

In figure 29 may be found our results for  $s$ , which we denote  $s_2$ , calculated in the same way from the first two Fourier coefficients of the observed polar energy distribution. The parameter  $s_2$  shows the same sort of dependence on  $\omega/\omega_p$  as that noted by Hasselmann *et al.* (1980), and the separate curves, grouped according to  $U_c/c_p$ , indicate that smaller  $s_2$  values (wider spreads) are associated with higher  $U_c/c_p$  values. The fitted lines to both front and rear spectral faces given by Hasselmann *et al.* (1980) are indicated on figure 29. While the dependence on  $\omega/\omega_p$  is qualitatively similar, Hasselmann *et al.* (1980) report generally smaller values of  $s$ , corresponding to broader spectra. Note that their data fall within the range  $1 < U_c/c_p < 2$ , so that comparison of their regression lines with the top curve of figure 29 is appropriate. In this range of  $U_c/c_p$  the results of Mitsuyasu *et al.* (1975) and Hasselmann *et al.* (1980) are in mutual agreement and suggest generally broader spectra than those reported here (figure 29). It is possible that the information contained in only the first few Fourier coefficients is insufficient to describe narrow directional spectra.

In practice, one's interest in the directional spread is generally focused on the 'energy containing' region. That is, the peak value and width at, say, half height are of more interest than the width of the tails of the spreading function. We may compute a value of  $s$  (which we shall call  $s_3$ ) which matches the half-height half-width  $\theta_{1/2}$  of the test model (§3.4) with that of the Mitsuyasu type spreading function. The estimates of  $s_3$  obtained in this way (figure 30) are much less scattered than those of  $s_2$ . Furthermore, the stratification with  $U_c/c_p$  has

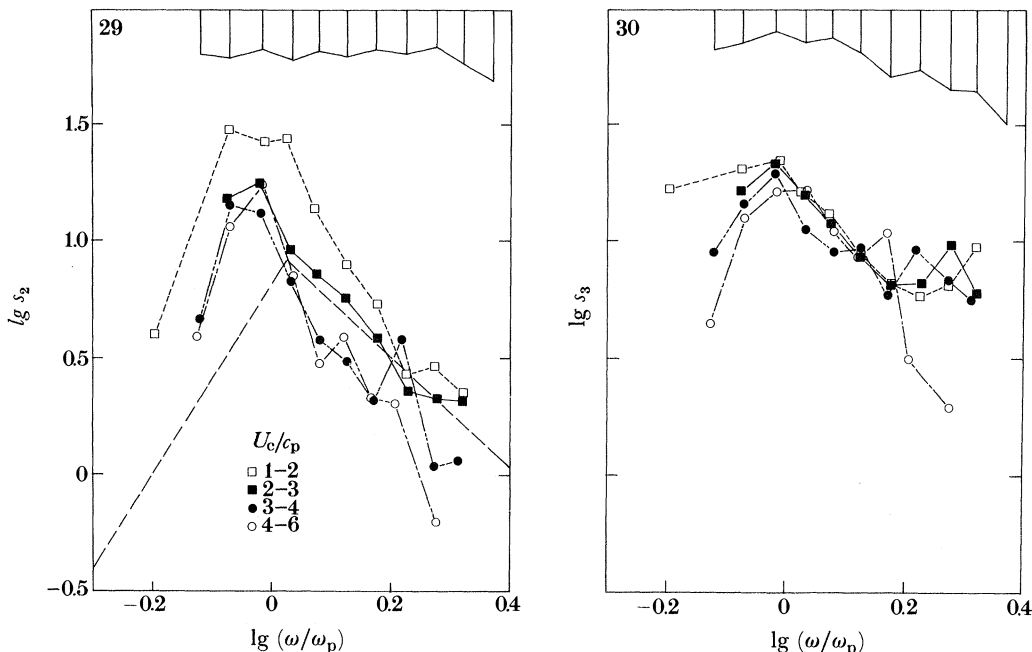


FIGURE 29. The  $s$  parameter, calculated from the first two Fourier coefficients, against  $\omega/\omega_p$ . The data are grouped in  $U_c/c_p$  classes. The dashed lines are taken from Hasselmann *et al.* (1980). The vertical bars at the top of the figure are an estimate of the 90 % confidence limits based on the standard error of the mean.

FIGURE 30. The  $s$  parameter calculated from the half-height of observed polar distributions.

disappeared, and the spreading function is now dependent only on  $\omega/\omega_p$ . The reduced scatter implies that the half-height width is a more stable description of the spreading than the first Fourier coefficients. The reason for this is probably that the half-height width is determined by the energy containing, and thus less noisy, part of the distribution, whereas the first Fourier coefficients are affected by the entire distribution. Possibly the tails of the directional spread are more influenced by changes in  $U/c$  than the peak is. In principle, energy from the wind will enter the distribution out to  $\theta = \arccos(c/U)$ ; while the peak of the directional spread, at least on the rear face of the frequency spectrum, is limited by dissipative processes and wave–wave interaction, i.e. processes less sensitive to  $U/c$ .

A further check of the appropriateness of the  $\cos^{2s}(\frac{1}{2}\theta)$  spreading function is graphed in figure 31. This figure compares the peak value of the test model  $A_0(L)$  with the peak of the  $\cos^{2s}(\frac{1}{2}\theta)$  distribution  $A_0(s)$ . The peaks of the latter are consistently too high by about 10 %. Based on this data set, it would seem that the  $\cos^{2s}(\frac{1}{2}\theta)$  spreading function consistently errs by overestimating the wave energy in the peak direction.

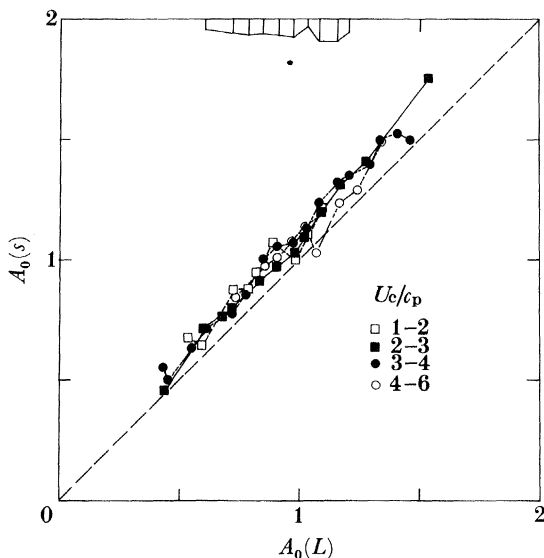


FIGURE 31. Comparison of the height of the peak of the  $\cos^{2s}(\frac{1}{2}\theta)$  distribution  $A_0(s)$  with the height of the test model  $A_0(L)$ . The distributions have equal integrals over  $\theta$  and the same half-height widths.

### 8.3. The $\operatorname{sech}^2(\beta\theta)$ spreading function

The failure of the various cosine distributions to model the observed polar distributions accurately has led us to consider yet another. The three-dimensional evolution of freely propagating, second-order Stokes gravity wave groups (Hui & Hamilton 1979; Hui 1980) indicates that an envelope soliton group propagating around the main wave direction is described by a hyperbolic secant. The distribution of wave energy in the direction transverse to the main wave direction behaves therefore like  $\operatorname{sech}^2$ . Since the envelope solitons survive interactions (Zhakarov 1968; Hui 1979, 1980), it seems not unreasonable to assume that the wave field consists of mainly (envelope) soliton groups. Then the directional distribution of the waves observed at a given point about the main wave direction must follow approximately a  $\operatorname{sech}^2(\beta\theta)$  distribution, at least for small  $\theta$ .

This suggestion from theory led to the testing of a spreading function for the distribution of energy (amplitude squared) of the form  $\text{sech}^2(\beta\theta)$ . The hyperbolic secant squared shape is preserved and the width of the spectral spread is determined by the parameter  $\beta$ . The dependence of  $\beta$  on  $\omega/\omega_p$ , from fitting to the half-height width of the test model, is graphed on logarithmic axes in figure 32. Here again, as in figure 30, the data for various values of  $U_c/c_p$  collapse on to a single average curve. In fact, in this sense there is little to choose between the  $\cos^{2s}(\frac{1}{2}\theta)$  and the  $\text{sech}^2(\beta\theta)$  distributions. However, a comparison of the peak values of the test model with the peak values of the  $\text{sech}^2(\beta\theta)$  distribution (figure 33) indicates that the  $\text{sech}^2(\beta\theta)$  distribution models the peak of the spreading function rather more faithfully than the cosine distribution (figure 31). In fact, the average overestimate of the wave energy in the peak direction is now only 2% for the  $\text{sech}^2(\beta\theta)$  distribution rather than 10% for the  $\cos^{2s}(\frac{1}{2}\theta)$  distribution.

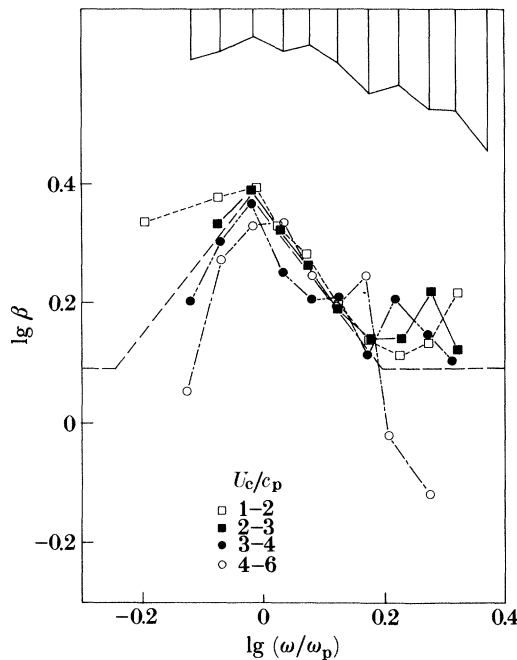


FIGURE 32. The  $\beta$  parameter derived from fitting  $\text{sech}^2(\beta\theta)$  to the half-height width of the test model.

Of course, the  $\text{sech}^2(\beta\theta)$  distribution extends beyond  $\pm\frac{1}{2}\pi$ , and our observed polar spectra are generally contained within this angular region. However, values of  $\beta$  are generally larger than 1.2 so that at  $\pm\frac{1}{2}\pi$  the spreading function is less than 9% of its peak value and less than 5% of the energy is outside of the range  $-\frac{1}{2}\pi < \theta < \frac{1}{2}\pi$ .

In figure 32 the dashed lines are a convenient representation of  $\beta$ :

$$\left. \begin{aligned} \beta &= 2.44(\omega/0.95\omega_p)^{+1.3}; & 0.56 < \omega/\omega_p < 0.95, \\ \beta &= 2.44(\omega/0.95\omega_p)^{-1.3}; & 0.95 < \omega/\omega_p < 1.6, \\ \beta &= 1.24; & \text{otherwise.} \end{aligned} \right\} \quad (8.4)$$

The range of directional spread given by (8.4) is illustrated in figure 34. From the narrowest to the widest our wind-generated spectra expand by about a factor of 2.

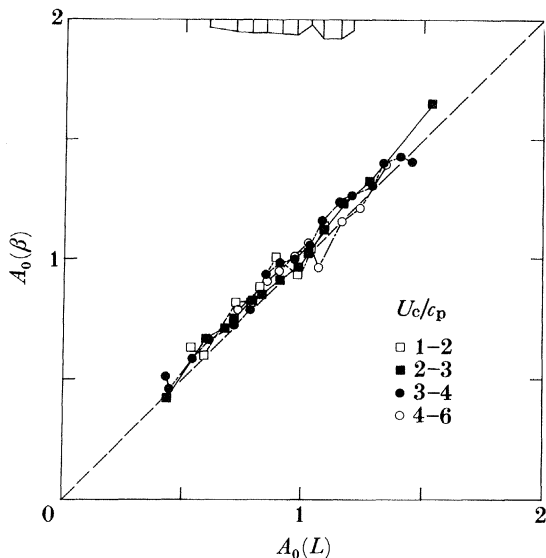


FIGURE 33. Comparison of the height of the peak of the  $\text{sech}^2(\beta\theta)$  distribution  $A_0(\beta)$  with the height of the test model  $A_0(L)$ .

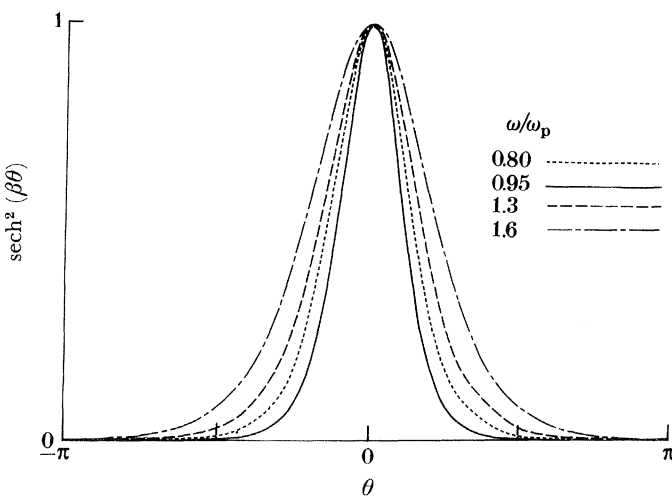


FIGURE 34. The  $\text{sech}^2(\beta\theta)$  spreading function for various  $\omega/\omega_p$ .

#### 8.4. Dependence on $\omega/\omega_p$

Hasselmann *et al.* (1980) have previously noted that the spreading function is more sensitive to  $\omega/\omega_p$  than to  $U/c$ . They argue that this implies that nonlinear interactions are more important than direct wind input in establishing the spectral shape. Our observations strengthen and extend theirs in that we find that the spreading function is adequately described by  $\omega/\omega_p$  alone in the  $U_c/c_p$  and  $\omega/\omega_p$  ranges of  $1 < U_c/c_p < 4$ ;  $0.8 < \omega/\omega_p < 1.6$ . However, we caution against the use of this result to establish which of the three source functions, wind input, nonlinear interactions or dissipation, is dominant in establishing the spectral shape of the rear face. It seems likely that all three source functions will depend on both  $U/c$  and  $\omega/\omega_p$  since, as we have shown, steepness is affected by both of these, and all three source functions are steepness dependent.

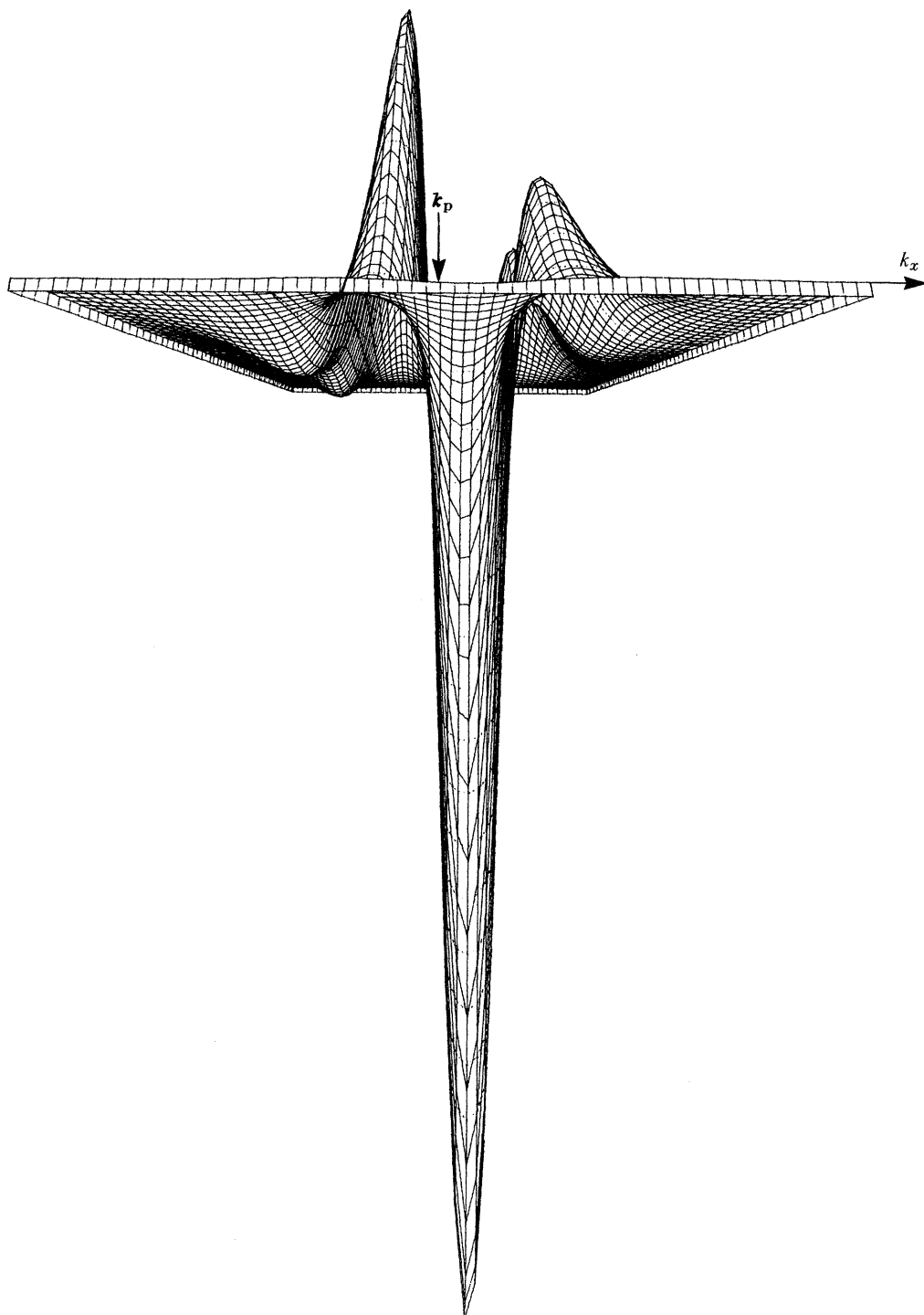


FIGURE 35. Rate of transfer of action density  $dN/dt$  due to nonlinear interaction of waves in a gaussian spectrum of spectral width 0.3, calculated from the theory of Dungey & Hui (1979). The horizontal plane is the expanded wavenumber plane relative to the spectral peak  $\mathbf{k}_p$ . The vertical scale is arbitrary. This perspective view is along the  $k_y$  axis and at  $10^\circ$  below the wavenumber plane.

In view of the dominance of  $\omega/\omega_p$  in the description of the spreading function it would not be surprising to find that its effect is felt in the frequency spectrum as well. In fact, the broadening of the directional spectrum away from the peak tends to whiten the frequency spectrum. This is, in effect, the behaviour of the rear face noted in §5.2, where the rear face of the frequency spectrum was shown to depend on

$$\omega^{-4}\omega_p^{-1}\alpha(U/c_p).$$

This empirical result could be realized by simple dimensional considerations if the peak frequency and wind speed are included in the list of relevant parameters:  $\Phi_r, g, U, \omega, \omega_p$ ; where  $\Phi_r(\omega)$  is the energy density on the rear face of the spectrum. Appropriate non-dimensional groups of these parameters are:  $\Phi_r \omega^5/g^2, \omega/\omega_p, U/c_p$ , and the spectrum is of the form

$$\phi_r(\omega) = g^2\omega^{-5}G(\omega/\omega_p, U/c_p). \quad (8.5)$$

The measurements described in §5 reveal that

$$G(\omega/\omega_p, U/c_p) = \alpha(U/c_p)\omega/\omega_p. \quad (8.6)$$

### 8.5. The directional spread of the forward face

It has been reported (Mitsuyasu *et al.* 1975; Hasselmann *et al.* 1980) that the spectra tend to be most narrow near the peak frequency. While this is true of our data as well (figures 27 and 28), we note that the maximum in our  $s$  or  $\beta$  values (figures 29 and 32) is displaced slightly but distinctly to the low frequency side of the peak frequency at about  $\omega/\omega_p = 0.95$ . In other words, the narrowest spreads occur on the forward face of the frequency spectrum. Hasselmann *et al.* (1973) first showed that the growth of the forward face of wind-wave spectra can be attributed to nonlinear wave-wave interactions; a conclusion that was further substantiated by the analytical calculations of Dungey & Hui (1979) for narrow spectra. This implies that the shape (and hence the angular spreading) of the three-dimensional wave spectrum  $X(\mathbf{k}, \omega)$  for  $\omega < \omega_p$  must be determined predominantly by the energy transfer due to nonlinear wave-wave interactions, the (direct) energy input from the wind and the energy loss due to whitecapping being relatively unimportant in this region. Systematic calculations by Dungey & Hui show that the energy transfer rate of a typical narrow wind-wave spectrum is of the shape given in figure 35. It is seen that there is a highly concentrated energy gain at wavenumbers slightly below  $k_p$  and in the mean wave direction. This may be responsible for the smallest angular spread occurring at a frequency slightly below the peak frequency since wind input, perhaps caused by random pressure fluctuations (Phillips 1957), would broaden the spectrum somewhat away from the area of strong nonlinear transfer. Some support for this explanation is provided by the numerical calculations of Sell & Hasselmann (1972) reported in Hasselmann *et al.* (1973) for the mean JONSWAP spectrum, in which the positive peak of the nonlinear transfer occurs at about  $\omega/\omega_p = 0.95$ , or just where we observe the narrowest directional distributions.

## 9. CONCLUDING REMARKS

Based on the idea of Barber (1963), a numerical method has been developed for computing the three-dimensional wind-generated wave spectrum  $X(\mathbf{k}, \omega)$  from an array of wave staffs. Essentially, the method applies the known array transfer function to the observed wavenumber spectrum to reveal the actual wavenumber spectrum. Wave records were obtained from a tower

in Lake Ontario that commanded fetches of 1.1 to 300 km, and from the C.C.I.W. wind-wave flume at a fetch of 50 m. The array consisted of 14 wave staffs and extended over 28 m in the lake and 1 m in the laboratory. Based on the analysis of 84 steady-state runs from the lake and 7 from the laboratory that covered a range of wind speed component to peak wave speed ratio ( $U_c/c_p$ ) of from 0.8 to 17, the following general conclusions are drawn.

The rear face or equilibrium range of the frequency spectra in both field and laboratory conditions is well described by an  $\omega^{-4}\omega_p^{-1}$  law for  $1.5 < \omega/\omega_p < 3.5$ . Accordingly, a new (modified JONSWAP) parametric spectral distribution is proposed, and the new equilibrium range, peak enhancement and peak width parameters ( $\alpha$ ,  $\gamma$  and  $\sigma$ ) are found to be functions of  $U_c/c_p$ .

The peak wave and wind directions are often quite different and the difference was correlated with the fetch gradient about the wind direction. An empirical formula based on a similarity argument is given which explains the observed difference between wave and wind directions. The formula can be used as a predictive tool in deducing steady-state wave directions from meteorological information.

In general, the observed phase speeds under natural conditions are slightly in excess of the linear dispersion relation for infinitesimal amplitude waves. The excess is explained satisfactorily by the amplitude dispersion effects of the Stokes wave. Significant energy was detected in the bound harmonics of the laboratory waves. Within the accuracy of these measurements bound harmonics could not be detected in the field data, although they must exist to produce the observed amplitude dispersion. From the laboratory data it was demonstrated that the ratio of the energy in the bound harmonics to the free waves at twice the peak frequency increases with  $U/c_p$ . Beyond  $U/c_p = 9.0$  it exceeds unity, i.e. bound harmonics dominate the spectrum near  $\omega/\omega_p = 2$ .

The angular spreading of wave energy is found to be smallest at a frequency  $\omega_s$  about 5% less than the peak frequency  $\omega_p$ . The spreading increases both as  $\omega$  increases and decreases from  $\omega_s$ . The spreading is best described by  $\text{sech}^2(\beta\theta)$  in which  $\beta$  is found to depend solely on  $\omega/\omega_p$ .

Emerging from this is a rather tidy description of the wind-generated wave spectrum, in which the energy level at any frequency  $\omega$  depends on the frequency itself, the position of that frequency in the spectrum ( $\omega/\omega_p$ ) and on the intensity of wind input  $U/c$ , while the directional spreading is related only to  $\omega/\omega_p$ .

We reproduce here our description of the wind-generated deep water directional spectrum in a form amenable to immediate application in wave forecasting and engineering design calculations:

$$F(\omega, \theta) = \frac{1}{2}\Phi(\omega)\beta \text{sech}^2\beta\{\theta - \bar{\theta}(\omega)\}, \quad (9.1)$$

where  $\bar{\theta}$  is the mean wave direction and

$$\left. \begin{aligned} \beta &= 2.61(\omega/\omega_p)^{+1.3}; & 0.56 < \omega/\omega_p < 0.95, \\ \beta &= 2.28(\omega/\omega_p)^{-1.3}; & 0.95 < \omega/\omega_p < 1.6, \\ \beta &= 1.24; & \text{otherwise.} \end{aligned} \right\} \quad (9.2)$$

The frequency spectrum is:

$$\Phi(\omega) = \alpha g^2 \omega^{-5} (\omega/\omega_p) \exp\left\{-\left(\frac{\omega_p}{\omega}\right)^4\right\} \gamma^r, \quad (9.3)$$

$$\alpha = 0.006(U_c/c_p)^{0.55}; \quad 0.83 < U_c/c_p < 5. \quad (9.4)$$

$$\gamma = \begin{cases} 1.7; & 0.83 < U_e/c_p < 1, \\ 1.7 + 6.0 \lg(U_e/c_p); & 1 \leq U_e/c_p < 5, \end{cases} \quad (9.5)$$

where  $\Gamma = \exp\{-(\omega - \omega_p)^2/2\sigma^2\omega_p^2\}$ ,

$$\sigma = 0.08[1 + 4/(U_e/c_p)^3]; \quad 0.83 < U_e/c_p < 5 \quad (9.6)$$

and  $U_e$  is the component of the average 10 m wind in the mean direction of the waves at the peak of  $\Phi(\omega)$ .

Finally, the fourth-order Stokes dispersion relation has been verified:

$$\omega^2 = gk\{1 + (ak)^2 + \frac{5}{4}(ak)^4\}, \quad (9.7)$$

where the  $U_e/c_p$  and frequency-dependent values of  $ak$  may be gleaned from figure 26.

We are indebted to the following members of the staff of the Canada Centre for Inland Waters for support during the preparation, realization and analysis of this experiment: M. Dick and M. Skafel (Management); E. Harrison, H. Savile, W. Gibson, S. Watson, C. Der, B. White, S. Beal, A. Pashley and J. Ford (Engineering); M. Pedrosa, J. Diaz and M. Larocque (technical), J. Carew, B. Macdonald, J. Roe and H. Don (logistics and diving); D. Beesley (data collection and archiving). We also thank L. Holthuijsen for useful criticism of the manuscript.

## REFERENCES

- Airy, G. B. 1845 Tides and waves. Arctic no. 192 in *Encyc. Metrop.*
- Banner, M. L. & Phillips, O. M. 1974 On small scale breaking waves. *J. Fluid Mech.* **65**, 647–657.
- Barber, N. F. 1963 The directional resolving power of an array of wave recorders. In *Ocean wave spectra*, pp. 137–150. Englewood Cliffs, N.J.: Prentice-Hall Inc.
- Barnett, T. P. & Kenyon, K. E. 1975 Recent advances in the study of wind waves. *Rep. Prog. Phys.* **38**, 667–729.
- Birch, K. N., Harrison, E. J. & Beal, S. 1976 A computer-based system for data acquisition and control of scientific experiments on remote platforms. In *Proc. Ocean 1976 Conf.*, Washington D.C., pp. 25B1–25B8.
- Borgman, L. E. 1979 Directional wave spectra from wave sensors. In *Ocean wave climate*, pp. 269–300. New York: Plenum.
- Brooke Benjamin, T. 1967 The instability of periodic wavetrains in nonlinear dispersive systems. *Proc. R. Soc. Lond. A* **299**, 59–75.
- Burling, R. W. 1959 *The spectrum of waves at short fetches*. *Dt. hydrogr. Z.* **12**(2), 45–117.
- Cote, L. J., Davis, J. O., Marks, W., McGough, R. J., Mehr, E., Pierson, W. J. Jr, Ropek, J. F., Stephenson, G. & Vetter, R. C. 1960 The directional spectrum of wind-generated sea as determined from data obtained by the stereo wave observation project. *Meteor. Pap.*, New York University, College of Engineering, vol. 2, no. 6, (88 pages).
- Davis, R. E. & Regier, L. 1977 Methods for estimating directional wave spectra from multi-element arrays. *J. mar. Res.* **35**, 453–477.
- Der, C. Y. & Watson, A. S. 1977 A high-resolution wave sensor array for measuring wave directional-spectra in the nearshore zone. In *Proc. Ocean 1977 Conf.*, Los Angeles, California, pp. 25D1–25D10.
- Donelan, M. A. 1978 Whitecaps and momentum transfer. In *Turbulent fluxes through the sea surface, wave dynamics and prediction*, pp. 273–287. New York: Plenum.
- Donelan, M. A. 1979 On the fraction of wind momentum retained by waves. In *Marine forecasting: predictability and modelling in ocean hydrodynamics*, pp. 141–159. Amsterdam: Elsevier.
- Donelan, M. A., Hamilton, J. & Hui, W. H. 1983 *Directional spectra of wind-generated waves*. (160 pages.). Canada Centre for Inland Waters, Burlington, Ontario.
- Donelan, M. A. & Pierson, W. J. 1983 The sampling variability of estimates of spectra of wind-generated gravity waves. *J. geophys. Res.* **88**, c7, 4381–4392.
- Dungey, J. C. & Hui, W. H. 1979 Nonlinear energy transfer in a narrow gravity-wave spectrum. *Proc. R. Soc. Lond. A* **368**, 239–265.
- Fontanel, A. & de Staerke, D. 1980 Spectres directionnels de vagues en mer du Nord. Images du radar de SEASAT. In *Climatologie de la mer, Conference internationale*, Paris, pp. 363–383. Paris: Éditions Techniques.
- Forristall, G. Z. 1981 Measurements of a saturated range in ocean wave spectra. *J. geophys. Res.* **86**, c9, 8075–8084.

- Fox, M. J. H. 1976 On the nonlinear transfer of energy in the peak of a gravity-wave spectrum. *Proc. R. Soc. Lond. A* **348**, 467–483.
- Garrett, J. 1969 Some new observations on the equilibrium region of the wind-wave spectrum. *J. mar. Res.* **27**, 273–277.
- Garrett, J. 1970 Field observations of frequency domain statistics and nonlinear effects in wind-generated ocean waves. (176 pages.) Thesis, University of British Columbia.
- Gill, G. C. 1975 Development and use of the Gill uvw anemometer. *Boundary Layer Meteorol.* **8**, 475–495.
- Hamilton, J., Hui, W. H. & Donelan, M. A. 1979 A statistical model for groupiness in wind waves. *J. geophys. Res.* **84**, c8, 4875–4884.
- Hasselmann, K. 1962 On the nonlinear energy transfer in a gravity wave spectrum. Part 1. *J. Fluid Mech.* **12**, 481–500.
- Hasselmann, K. 1963a On the nonlinear energy transfer in a gravity wave spectrum. Part 2. *J. Fluid Mech.* **15**, 273–281.
- Hasselmann, K. 1963b On the nonlinear energy transfer in a gravity wave spectrum. Part 3. *J. Fluid Mech.* **15**, 385–398.
- Hasselmann, K., Barnett, T. P., Bouws, E., Carlson, H., Cartwright, D. E., Enke, K., Ewing, J. A., Gienapp, H., Hasselmann, D. E., Kruseman, P., Meerburg, A., Müller, P., Olbers, D. J., Richter, K., Sell, W. & Walden, H. 1973 Measurements of wind-wave growth and swell decay during the Joint North Sea Wave Project (JONSWAP) (95 pages.). *Dt. hydrogr. Z.*, A8 (Suppl.), no. 12.
- Hasselmann, D. E., Dunckel, M. & Ewing, J. A. 1980 Directional wave spectra observed during JONSWAP 1973. *J. phys. Oceanogr.* **10**, 1264–1280.
- Holthuijsen, L. H. 1981 The directional energy distribution of wind generated waves as inferred from stereophotographic observations of the sea surface. Thesis, Delft University of Technology. (193 pages.) Rep. no. 81–2.
- Huang, N. E., Long, S. R. & Bliven, L. F. 1981a On the importance of significant slope in empirical wind-wave studies. *J. phys. Oceanogr.* **10**, 569–573.
- Huang, N. E., Long, S. R., Tung, C.-C., Yuen, Y. & Bliven, L. 1981b A unified two-parameter wave spectral model for a general sea state. *J. Fluid Mech.* **112**, 203–224.
- Hui, W. H. 1979 Exact envelope-soliton solutions of a two-dimensional nonlinear wave equation. *Z. angew. Math. Phys.* **30**, 929–936.
- Hui, W. H. 1980 Three-dimensional nonlinear evolution of water waves. In *Nonlinear partial differential equations in engineering and applied science* (ed. R. L. Sternberg, A. J. Kalinowski & J. S. Papadakis), pp. 167–187. New York: Marcel Dekker Inc.
- Hui, W. H. & Hamilton, J. 1979 Exact solutions of a three-dimensional nonlinear Schrödinger equation applied to gravity waves. *J. Fluid Mech.* **93**, 117–133.
- Hui, W. H. & Tenti, G. 1982 A new approach to steady flows with free surfaces. *Z. angew. Math. Phys.* **33**, 569–589.
- Irani, G. B., Gotwols, B. L. & Bjerkaas, A. W. 1981 Ocean wave dynamics test: results and interpretations. Rep. no. STD-R-537, The Johns Hopkins University, Applied Physics Laboratory. 202 pp.
- Kahma, K. K. 1981 A study of the growth of the wave spectrum with fetch. *J. phys. Oceanogr.* **11**, 1503–1515.
- Kinsman, B. 1960 Surface waves at short fetches and low wind speed – a field study. (581 pages.) Tech. Rep. no. 19. Chesapeake Bay Inst., Johns Hopkins University.
- Kitaigorodskii, S. A. 1962 Applications of the theory of similarity to the analysis of wind-generated wave motion as a stochastic process. *Bull. Acad. Sci. USSR Geophys. Ser.* 1, 105–117.
- Kitaigorodskii, S. A., Krasitskii, V. P. & Zaslavskii, M. M. 1975 On Phillips' theory of equilibrium range in the spectra of wind-generated gravity waves. *J. phys. Oceanogr.* **5**, 410–420.
- Komen, G. J. 1980 Nonlinear contributions to the frequency spectrum of wind-generated water waves. *J. phys. Oceanogr.* **5**, 779–790.
- Korvin-Kroukovsky, B. V. 1967 Further reflections on properties of sea waves developing along a fetch. *Dt. hydrogr. Z.* **2**, 7.
- Lake, B. M. & Yuen, H. C. 1978 A new model for nonlinear wind waves. Part 1. Physical model and experimental evidence. *J. Fluid Mech.* **88**, 33–62.
- Liu, P. C. 1971 Normalized and equilibrium spectra of wind waves in Lake Michigan. *J. phys. Oceanogr.* **1**, 249–257.
- Longuet-Higgins, M. S. 1969 On wave breaking and the equilibrium spectrum of wind-generated waves. *Proc. R. Soc. Lond. A* **310**, 151–159.
- Longuet-Higgins, M. S. 1976 On the nonlinear transfer of energy in the peak of the gravity-wave spectrum: a simplified model. *Proc. R. Soc. Lond. A* **347**, 311–328.
- Longuet-Higgins, M. S. 1977 Some effects of finite steepness on the generation of waves by wind. In *A voyage of discovery*, pp. 393–403. Oxford: Pergamon.
- Longuet-Higgins, M. S., Cartwright, D. E. & Smith, N. D. 1963 Observations of the directional spectrum of sea waves using the motions of a floating buoy. In *Ocean wave spectra*, pp. 111–136. Englewood Cliffs, N.J.: Prentice Hall, Inc.
- Longuet-Higgins, M. S. & Cokelet, E. D. 1976 The deformation of steep surface waves. I. A numerical method of computation. *Proc. R. Soc. Lond. A* **350**, 1–26.
- Longuet-Higgins, M. S. & Phillips, O. M. 1962 Phase velocity effects in tertiary wave interactions. *J. Fluid Mech.* **12**, 333–336.

- McLeish, W., Ross, D., Shuchman, R. A., Teleki, P. G., Hsiao, S. V., Shemdin, O. H. & Brown, W. E. Jr 1980 Synthetic aperture radar imaging of ocean waves: comparison with wave measurements. *J. geophys. Res.* **85**, c9, 5003–5011.
- Mitsuyasu, H. 1968 On the growth of the spectrum of wind generated waves, I. *Rep. Res. Inst. appl. Mech. Kyushu Univ.* **16**, 459–482.
- Mitsuyasu, H. 1969 On the growth of the spectrum of wind generated waves, II. *Rep. Res. Inst. appl. Mech. Kyushu Univ.* **17**, 235–248.
- Mitsuyasu, H., Kuo, Y.-Y. & Masuda, A. 1979 On the dispersion relation of random gravity waves, Part 2. An experiment. *J. Fluid Mech.* **92**, 731–749.
- Mitsuyasu, H., Tasai, F., Suhara, T., Mizuno, S., Ohkuso, M., Honda, T. & Rikiishi, K. 1975 Observations of the directional spectrum of ocean waves using a cloverleaf buoy. *J. phys. Oceanogr.* **5**, pp. 750–760.
- Pawka, S. S., Hsiao, S. V., Shemdin, O. H. & Inman, D. L. 1980 Comparisons between wave directional spectra from SAR and pressure sensor arrays. *J. geophys. Res.* **85**, c9, 4987–4995.
- Phillips, O. M. 1957 On the generation of waves by turbulent wind. *J. Fluid Mech.* **2**, 417–445.
- Phillips, O. M. 1958 The equilibrium range in the spectrum of wind-generated waves. *J. Fluid Mech.* **4**, 426–434.
- Phillips, O. M. 1960 On the dynamics of unsteady gravity waves of finite amplitude, Part I. *J. Fluid Mech.* **9**, 193–217.
- Phillips, O. M. 1977 *The dynamics of the upper ocean* (2nd edn). (336 pages.) Cambridge University Press.
- Phillips, O. M. 1980 Wave generation propagation and dissipation theory. In *Transcript of workshop on wind-wave hindcasting and forecasting models*, pp. 6–19. Gaithersburg, Md.: National Oceanic and Atmospheric Administration.
- Pierson, W. J. & Moskowitz, L. 1964 A proposed spectral form for fully developed wind seas based on the similarity theory of S. A. Kitaigorodskii. *J. geophys. Res.* **69**, 5181–5190.
- Plant, W. J. & Wright, J. W. 1980 Phase speeds of upwind and downwind travelling short gravity waves. *J. geophys. Res.* **85**, c6, 3304–3310.
- Ramamonjjarisoa, A. 1973 Sur l'évolution des spectres d'énergie des vagues de vent à fetchs courts. *Mém. Soc. R. Sci. Liège Ser. 6*, **6**, 47–66.
- Ramamonjjarisoa, A. 1974 Contribution à l'étude de la structure statistique et des mécanismes de génération des vagues de vent. Thesis, Université de Provence (Inst. Méch. Stat. de la Turbulence, no. A.O. 10023).
- Regier, L. A. & Davis, R. E. 1977 Observation of the power and directional spectrum of ocean surface waves. *J. mar. Res.* **35**, 433–451.
- Rikiishi, K. 1978a A new method for measuring the directional wave spectrum. I. Description. *J. phys. Oceanogr.* **8**, 508–517.
- Rikiishi, K. 1978b A new method for measuring the directional wave spectrum. II. Measurements of the directional spectrum and phase velocity of laboratory wind waves. *J. phys. Oceanogr.* **8**, 518–529.
- Schuler, D. L. 1978 Remote sensing of directional gravity wave spectra and surface currents using microwave dual-frequency radar. *Radio Sci.* **13**, 321–331.
- Sell, W. & Hasselmann, K. 1972 Computations of nonlinear energy transfer for JONSWAP and empirical wind wave spectra. Rep. Inst. Geophys., Univ. Hamburg.
- Simons, T. J. 1974 Verification of numerical models of Lake Ontario, I. Circulation in spring and early summer. *J. phys. Oceanogr.* **4**, 507–523.
- Simons, T. J. 1975 Verification of numerical models of Lake Ontario, II. Stratified circulations and temperature changes. *J. phys. Oceanogr.* **5**, 98–110.
- Stewart, R. W. 1974 The air-sea momentum exchange. *Boundary Layer Meteorol.* **6**, 151–167.
- Stewart, R. H. & Joy, J. W. 1974 HF radio measurements of surface currents. *Deep Sea Res.* **21**, 1039–1049.
- Stokes, G. G. 1847 On the theory of oscillatory waves. *Trans. Camb. phil. Soc.* **8**, 441–455.
- Sturm, G. V. & Sorrell, F. Y. 1973 Optical wave measurement technique and experimental comparison with conventional wave height probes. *Appl. Optics* **12**, 1928–1933.
- Toba, Y. 1973 Local balance in the air-sea boundary processes, III. On the spectrum of wind waves. *J. oceanogr. Soc. Japan* **29**, 209–220.
- Trizna, D. B., Bogle, R. W., Moore, J. C. & Howe, C. M. 1980 Observation by H. F. Radar of the Phillips resonance mechanism for generation of wind waves. *J. geophys. Res.* **85**, c9, 4946–4956.
- Tyler, G. L., Teague, C. C., Stewart, R. H., Peterson, A. M., Munk, W. H. & Joy, J. W. 1974 Wave directional spectra from synthetic aperture observations of radio scatter. *Deep Sea Res.* **21**, 989–1016.
- Webb, D. J. 1978 Nonlinear transfers between sea waves. *Deep Sea Res.* **25**, 279–298.
- Whitham, G. B. 1967 Nonlinear dispersion of water waves. *J. Fluid Mech.* **27**, 399–412.
- Whitham, G. B. 1974 *Linear and nonlinear waves*. (636 pages.) New York: John Wiley & Sons.
- Wu, J. 1975 Wind-induced drift currents. *J. Fluid Mech.* **68**, 49–70.
- Wu, J. 1977 Directional slope and curvature distributions of wind waves. *J. Fluid Mech.* **79**, 463–480.
- Zakharov, V. E. 1968 Stability of periodic waves of finite amplitude on the surface of a deep fluid. *Soviet Physics appl. Mech. tech. Phys.* **4**, 190–194.
- Zakharov, V. E. & Filonenko, N. N. 1967 Energy spectrum for stochastic oscillations of the surface of a liquid. *Soviet Phys. Dokl.* **11**, 881–883.

anemometer bivane

Downloaded from <http://rsta.royalsocietypublishing.org/> on January 11, 2015

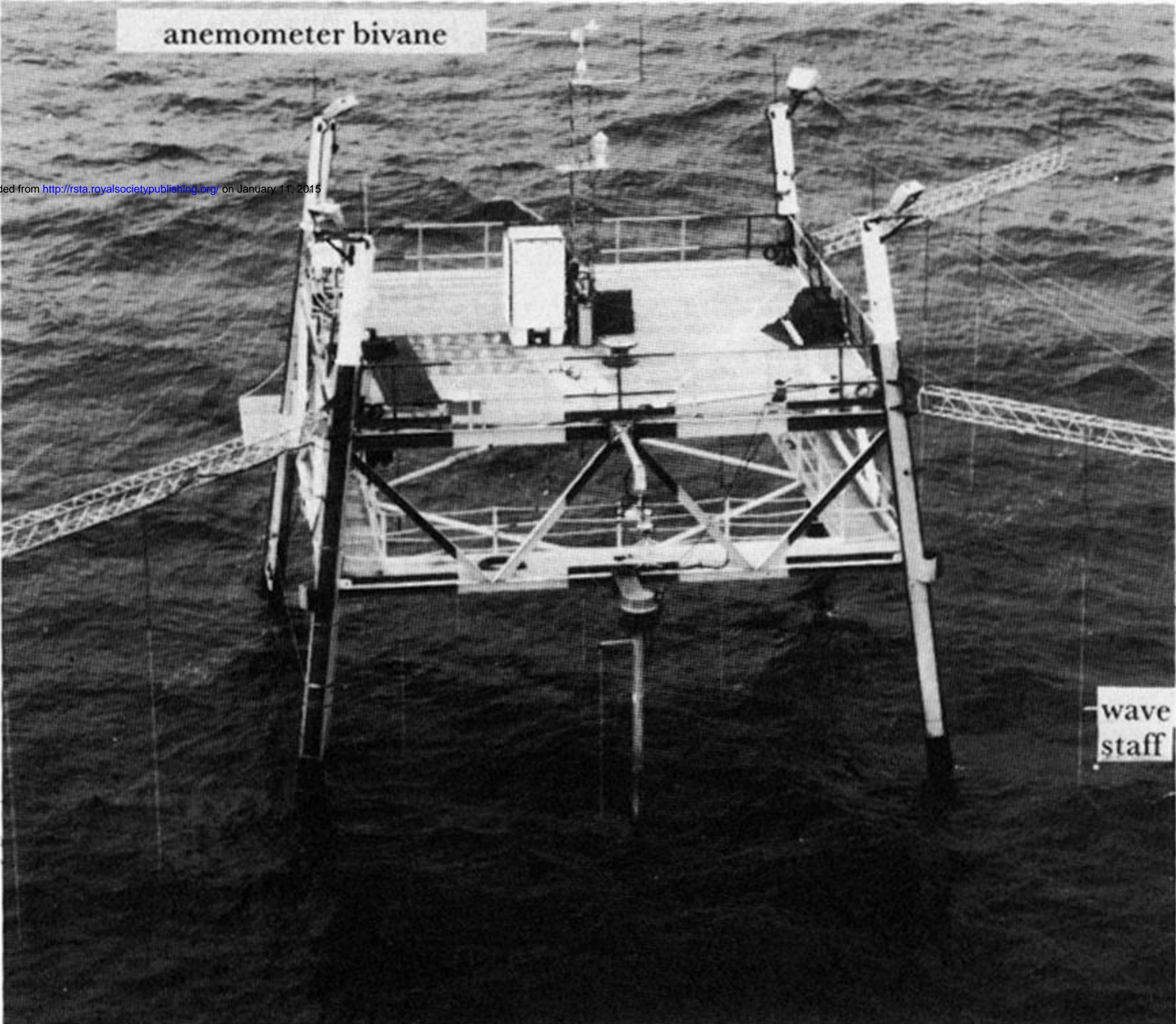


FIGURE 2. Photograph of the research tower. The wave staffs can be seen suspended from the tower itself and from its extensions in three directions. Meteorological instruments are mounted on a mast at the centre and the measuring and communications devices are housed in the box at the foot of the mast.